Transition Metal Complexes for Photovoltaic and Light Emitting Applications

M. K. Nazeeruddin (✉) · M. Grätzel

Laboratory for Photonics and Interfaces,
Institute of Molecular and Biological Chemistry, School of Basic Sciences,
Swiss Federal Institute of Technology, 1015 Lausanne, Switzerland
MdKhaja.Nazeeruddin@epfl.ch

Abstract The aim of this chapter is to give an in-depth analysis of transition metal complexes that are useful in conversion of solar energy into electricity, and in organic light emitting diodes. In the first part we discuss the historical background of sensitization

phenomenon, operating principles of dye-sensitized solar cells, tuning of photophysical and electrochemical properties of sensitizers, evolution of photovoltaic performance, present status and future prospects for dye-sensitized solar cells. In the second part, we elucidate the modulation of phosphorescent color and quantum yields in neutral, cationic, and anionic iridium complexes and their application in light emitting devices.

Keywords Dye-sensitized solar cells · Iridium triplet emitters · Light emitting electrochemical cells · OLED · Photovoltaic · Ruthenium sensitizers

Abbreviations

CIGS	Copper indium gallium selenide
dcbiq	4,4′-Dicarboxy-2,2′-biquinoline
dcbpy	4,4′-Dicarboxy-2,2′-bipyridine
DSC	Dye-sensitized solar cell
$Fc^{+/0}$)	Ferrocenium/ferrocene
FF	Fill factor
HOMO	Highest occupied molecular orbitals
IPCE	Incident monochromatic photon-to-current conversion efficiency
LUMO	Lowest unoccupied molecular orbitals
MLCT	Metal-to-ligand charge transfer
OLED	Organic light emitting diode
ppy	2-Phenylpyridine
SCE	Saturated calomel electrode
UV-Vis	Ultraviolet-visible
J_{sc}	Short circuit current
V_{oc}	Open-circuit potential

1
Dye-Sensitized Solar Cells

1.1
History of Dye Sensitization

The history of the sensitization of semiconductors to light of wavelength longer than that corresponding to the band gap is an interesting convergence of photography and photoelectrochemistry, both of which rely on photoinduced charge separation at a liquid–solid interface [1]. The silver halides used in photography have band gaps of the order of 2.7–3.2 eV and are therefore insensitive towards much of the visible spectrum, as are the metal oxide films now used in dye-sensitized solar cells.

The first panchromatic film, able to render the image of a scene realistically into black and white, followed on the work of Vogel in Berlin after 1873, [2] in which he associated dyes with the halide semiconductor grains. The first sensitization of a photoelectrode was reported shortly thereafter, using a similar chemistry [3]. However, the clear recognition of the parallels between the

two procedures – a realization that the same dyes in principle can function in both systems [4] and a verification that their operating mechanism is by injection of electrons from photoexcited dye molecules into the conduction band of the n-type semiconductor substrates – date to the 1960s [5]. In subsequent years the idea developed that the dye could function most efficiently if chemisorbed on the surface of the semiconductor [6, 7]. The concept of using dispersed particles to provide a sufficient interface area emerged [8], and was subsequently employed for photoelectrodes [9].

Titanium dioxide became the semiconductor of choice for the photoelectrode. The material has many advantages for sensitized photochemistry and photoelectrochemistry: it is a low cost, widely available, nontoxic and biocompatible material, and as such is even used in health care products as well as in domestic applications such as paint pigmentation. Initial studies employed [Ru(4,4'-dicarboxylic acid 2,2'-bipyridine ligand)$_3$] (**1**) as the sensitizer for photochemical studies. Progress thereafter, until the announcement in 1991 [10] of a sensitized electrochemical photovoltaic device with a conversion efficiency of 7.1% under solar illumination, was incremental, through the combining of a synergy of structure, substrate roughness and morphology, dye photophysics, and electrolyte redox chemistry. That evolution has continued progressively since then, with certified efficiencies now over 11% [11].

The dye-sensitized solar cell technology developed at the EPFL contains broadly five components:

1. Conductive mechanical support
2. Semiconductor film
3. Sensitizer
4. Electrolyte containing I$^-$/I$_3^-$ redox couple
5. Counter electrode with a triodide reduction catalyst

A cross-section of the dye-sensitized solar cell is shown in Fig. 1. The total efficiency of the dye-sensitized solar cell depends on the optimization and compatibility of each of these constituents [12]. To a large extent, the nanocrys-
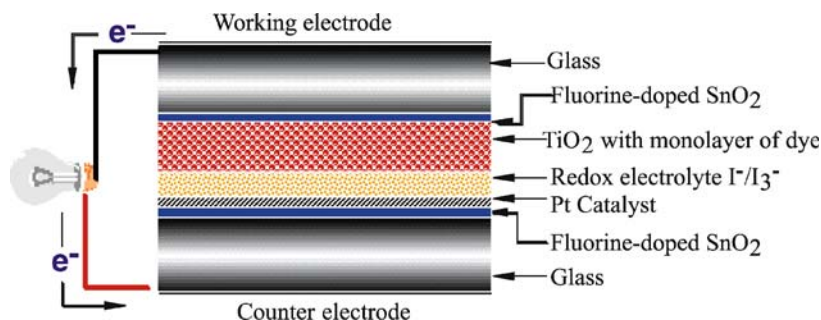

Fig. 1 Schematic representation of the cross-section of a dye-sensitized solar cell

talline semiconductor film technology along with the dye spectral responses is mainly responsible for the high efficiency [12]. A way to successfully trap solar radiation is by a sensitizer molecule anchored to a rough titania surface, analogous to the light-absorbing chlorophyll molecule found in the nature. The high surface area and the thickness of the semiconductor film yield increased dye optical density resulting in efficient light harvesting [13].

1.2
Operating Principles of the Dye-Sensitized Solar Cell

The details of the operating principles of the dye-sensitized solar cell are given in Fig. 2. The photoexcitation of the metal-to-ligand charge transfer (MLCT) of the adsorbed sensitizer (Eq. 1) leads to injection of electrons into the conduction band of the oxide (Eq. 2). The oxidized dye is subsequently reduced by electron donation from an electrolyte containing the iodide/triiodide redox system (Eq. 3). The injected electron flows through the semiconductor network to arrive at the back contact and then through the external load to the counter
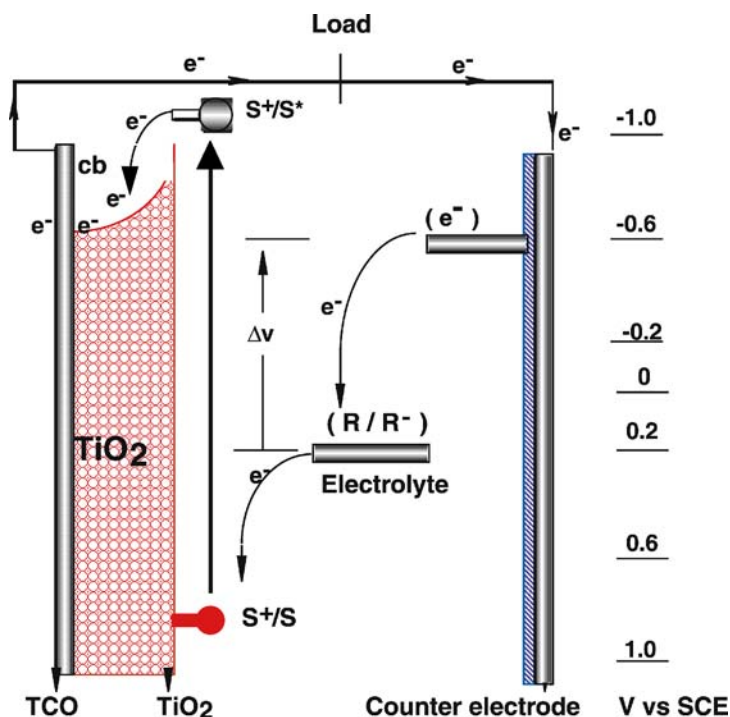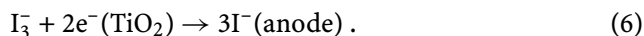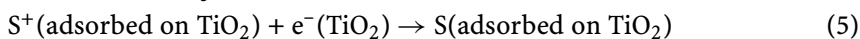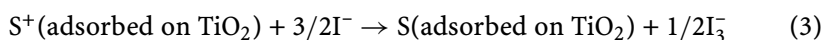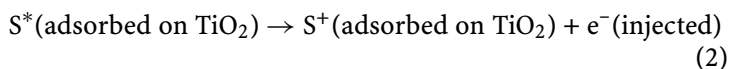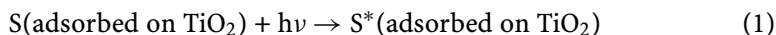

Fig. 2 Operating principles and energy level diagram of dye-sensitized solar cell. $S/S^+/S^*$ represent the sensitizer in the ground, oxidized, and excited state, respectively. R/R^- represent the redox mediator (I^-/I_3^-)

electrode. At the counter electrode, reduction of triiodide in turn regenerates iodide (Eq. 4), which completes the circuit. With a closed external circuit and under illumination, the device then constitutes a photovoltaic energy conversion system, which is regenerative and stable. However, there are undesirable reactions, which are that the injected electrons may recombine either with oxidized sensitizer (Eq. 5) or with the oxidized redox couple at the TiO$_2$ surface (Eq. 6), resulting in losses in the cell efficiency.

$$S(\text{adsorbed on TiO}_2) + h\nu \rightarrow S^*(\text{adsorbed on TiO}_2) \tag{1}$$

$$S^*(\text{adsorbed on TiO}_2) \rightarrow S^+(\text{adsorbed on TiO}_2) + e^-(\text{injected}) \tag{2}$$

$$S^+(\text{adsorbed on TiO}_2) + 3/2I^- \rightarrow S(\text{adsorbed on TiO}_2) + 1/2I_3^- \tag{3}$$

$$I_3^- + 2e^-(\text{cathode}) \rightarrow 3I^-(\text{cathode}) \tag{4}$$

$$S^+(\text{adsorbed on TiO}_2) + e^-(\text{TiO}_2) \rightarrow S(\text{adsorbed on TiO}_2) \tag{5}$$

$$I_3^- + 2e^-(\text{TiO}_2) \rightarrow 3I^-(\text{anode}) \,. \tag{6}$$

At the heart of the system is a mesoporous oxide layer composed of nanometer-sized particles, which have been sintered together to allow electronic conduction to take place. The material of choice has been TiO$_2$ (anatase) although alternative wide band gap oxides such as ZnO, SnO$_2$ and Nb$_2$O$_5$ have also been investigated. Attached to the surface of the nanocrystalline film is a monolayer of a sensitizer. The high surface area of the mesoporous metal oxide film is critical to efficient device performance as it allows strong absorption of solar irradiation to be achieved by only a monolayer of adsorbed sensitizer. The use of a dye monolayer avoids any requirement for excited state (or "exciton") diffusion to the dye/metal oxide interface. It also avoids the acceleration in non-radiative excited state decay to ground state that is often associated with thicker molecular films. The use of a mesoporous film results in a dramatic enhancement of the interfacial surface area by more than 1000-fold for a 10 mm thick film. This leads to high visible light absorbance from the monolayer of adsorbed dye (a dye monolayer adsorbed to a flat interface exhibits only negligible light absorption as the optical absorption cross-sectional area for molecular dyes are typically two to three orders of magnitude smaller than their physical cross-sections). The high surface area of such mesoporous films does however have a significant downside, as it also enhances interfacial charge recombination losses, a topic we return to in more detail in Sect. 1.5.1.4.

1.3
Device Fabrication

Dye-sensitized solar cells are typically fabricated upon transparent conducting glass substrates, enabling light irradiance through this substrate under

photovoltaic operation. The conductive coating typically used is fluorine-doped SnO_2 (fluorine tin oxide, FTO), preferred over its indium-doped analogue (ITO) for reasons of lower cost and enhanced stability. Prior to deposition of the mesoporous TiO_2 film, a dense TiO_2 film may be deposited to act as a hole-blocking layer, preventing recombination (shunt resistance) losses between electrons in the FTO and oxidized redox couple.

The TiO_2 nanoparticles are typically fabricated by the aqueous hydrolysis of titanium alkoxide precursors, followed by autoclaving at temperatures of up to 240 °C to achieve the desired nanoparticle dimensions and crystallinity (anatase) [14]. The nanoparticles are deposited as a colloidal suspension by screen printing or doctor blading, followed by sintering at $\sim$ 450 °C to ensure good interparticle connectivity. The porosity of the film is controlled by the addition of an organic filler (e.g., carbowax) to the suspension prior to deposition; this filler is subsequently burnt off during the sintering step. Figure 3 shows a scanning electron micrograph of a typical mesoporous TiO_2 film. Typical film thicknesses are 5–20 μm, with TiO_2 mass of about 1–4 mg cm^{-2}, film porosity 50–65%, average pore size 15 nm, and particle diameters 15–20 nm.

The classic sensitizer dye employed in DSC is a Ru(II) bipyridyl dye, *cis*-bis(isothiocyanato)-bis(2,2′-bipyridyl-4,4′-dicarboxylato)-Ru(II), often referred to as "N3", or in its partially deprotonated form (a di-tetrabutyl-ammonium salt) as N719. The structure of these dyes are shown in **2** and **26**. The incorporation of carboxylate groups allows immobilization of sensitizer to the film surface via the formation of bidendate coordination and ester linkages, whilst the (– NCS) groups enhance the visible light absorption. Adsorption of the dye to the mesoporous film is achieved by simple immersion of the film in a solution of dye, which results in the adsorption of a dye monolayer to the film surface. The counter electrode is fabricated from FTO-coated glass, with the addition of a Pt catalyst to catalyze the reduc-
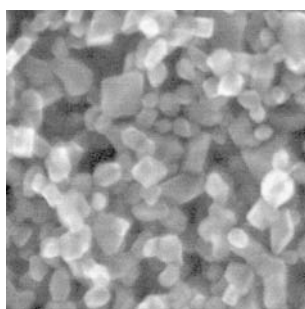

Fig. 3 Scanning electron microscope image of a typical mesoscopic TiO_2 film employed in DSC. Note the bipyramidal shape of the particles having (101) oriented facets exposed. The average particle size is 20 nm

tion of the triiodide at this electrode. Electrical contact between working and counter electrode is achieved by the redox electrolyte, with capillary forces being sufficient to ensure that the electrolyte efficiently penetrates the film pores.

1.4
Incident Photon to Current Efficiency and Open Circuit Photovoltage

The incident monochromatic photon-to-current conversion efficiency (IPCE), defined as the number of electrons generated by light in the external circuit divided by the number of incident photons as a function of excitation wavelength, is expressed in Eq. 7 [15]. The open-circuit photovoltage is determined by the energy difference between the Fermi level of the solid under illumination and the Nernst potential of the redox couple in the electrolyte (Fig. 2). However, the experimentally observed open-circuit potential for various sensitizers is smaller than the difference between the conduction band edge and the redox couple, probably due to the competition between electron transfer and charge recombination pathways. Knowledge of the rates and mechanisms of these competing reactions are vital for the design of efficient sensitizers and, thereby, improvement of the solar devices [16–18].

$$\mathrm{IPCE} = \frac{[(1.25 \times 10^3) \times \text{ photocurrent density } [\mathrm{mA\,cm^{-2}}]]}{[\text{wavelength } [\mathrm{nm}] \times \text{ photon flux } [\mathrm{W\,m^{-2}}]]}\,. \tag{7}$$

Power output from the DSC requires not only efficient charge collection by the electrodes, but the generation of a photovoltage corresponding to a free energy difference between the working and counter electrodes. In the dark at equilibrium, the Fermi energy of the TiO_2 electrode (corresponding to the free energy of electrons in this film after thermalization) equilibrates with the midpoint potential of the redox couple, resulting in zero output voltage. Under these conditions, the TiO_2 Fermi level lies deep within the band gap of the semiconductor, and the film is effectively insulating, with a negligible electron density in the TiO_2 conduction band. Photoexcitation results in electron injection into the TiO_2 conduction band and the concomitant hole injection into (oxidation of) the redox electrolyte. The high concentrations of oxidized and reduced redox couple present in the electrolyte in the dark mean that this photoxidation process does not result in a significant change in chemical potential of the electrolyte, which remains effectively fixed at its dark, resting value. In contrast, electron injection into the TiO_2 conduction band results in a dramatic increase in electron density (from the order of 10^{13} cm^{-3} to 10^{18} cm^{-3}), raising the TiO_2 Fermi level (technically the electron quasi-Fermi level) towards the conduction band edge, and allowing the film to become conducting. This shift of the TiO_2 Fermi level under irradiation increases the free energy of injected electrons and is responsible for the generation of the photovoltage in the external circuit.

The midpoint potential of the redox couple is given by the Nernst equation, and is therefore dependent upon the relative concentrations of iodide and iodine. The concentrations of these species required for efficient device function are in turn constrained by kinetic requirements of dye regeneration at the working electrode, and iodide regeneration at the counter electrode, as discussed below. Typical concentrations of these species are in the range 0.5–1.2 M iodide and 10–200 mM iodine, constraining the midpoint potential of this electrolyte to ∼ 0.4 V vs NHE. It should furthermore be noted that in the presence of excess iodide, the iodine is primarily present in the form I_3^-, resulting in this electrolyte often being referred to as an iodide/triiodide redox couple.

The overall conversion efficiency (η) of the dye-sensitized solar cell is determined by the photocurrent density (j_{ph}), the open circuit potential (V_{oc}), the fill factor (FF) of the cell and the intensity of the incident light (I_s), (Eq. 8) [19].

$$\eta_{global} = j_{ph} V_{oc} FF/I_s \tag{8}$$

1.5
Molecular Sensitizers

The photophysical and photochemical properties of 4d and 5d metal complexes containing polypyridyl ligands have been thoroughly investigated over the last three decades. The main thrust behind these studies was to understand the energy and electron transfer processes in the excited states and to apply this knowledge to potential practical applications such as dye-sensitized solar cells, organic light-emitting diodes, and light-emitting electrochemical cells. Particularly, there is currently considerable interest in Ru(II) polypyridyl complexes because of their applications in nanocrystalline TiO_2-based solar cells [20–23]. The choice of Ru metal is of interest for a number of reasons:

- Because of its octahedral geometry specific ligands can be introduced in a controlled manner
- The photophysical and electrochemical properties of Ru complexes can be tuned in a predictable way
- The Ru metal center possess stable and accessible oxidation states from I to III

The ground and the excited state electrochemical and photophysical properties of these complexes play an important role in the charge transfer dynamics at the interfaces.

The optimal sensitizer for the dye-sensitized solar cell should be panchromatic, i.e., absorb visible light of all colors. Ideally, all photons below a threshold wavelength of about 920 nm should be harvested and converted to electric current. This limit is derived from thermodynamic considerations, showing

that the conversion efficiency of any single-junction photovoltaic solar converter peaks at approximately 33% near a threshold energy of 1.4 eV [24, 25]. Also, the sensitizer should have suitable ground and excited state redox properties, and interlocking groups for grafting the dye on the semiconductor surface. These ascertain intimate electronic coupling between its excited state wave function and the conduction band manifold of the semiconductor [26, 27].

Molecular engineering of Ru complexes that can act as panchromatic charge transfer sensitizers for TiO_2-based solar cells presents a challenging task as several requirements have to be fulfilled by the dye that are very difficult to be met simultaneously. The lowest unoccupied molecular orbitals (LUMO) and the highest occupied molecular orbitals (HOMO) have to be maintained at levels where photoinduced electron transfer in the TiO_2 conduction band and regeneration of the dye by iodide can take place at practically 100% yield. This greatly restricts the options available to accomplish the desired red shift of the MLCT transitions to about 900 nm.

The spectral and redox properties of Ru polypyridyl complexes can be tuned in two ways. Firstly, by introducing a ligand with a low-lying π^* molecular orbital and secondly by destabilization of the metal t_{2g} orbital through the introduction of a strong donor ligand. Meyer et al. have used these strategies to considerably tune the MLCT transitions in Ru complexes [28]. Heteroleptic complexes containing bidentate ligands with low-lying π^* orbitals, together with others having strong σ donating properties, indeed show impressive panchromatic absorption properties. However, the extension of the spectral response into the near IR was gained at the expense of shifting the LUMO to lower levels, from where charge injection into the TiO_2 conduction band can no longer occur [29].

Near-infrared response can also be gained by upward shifting of the Ru t_{2g} (HOMO) levels. However, it turns out that the mere introduction of strong σ donor ligands into the complex often does not lead to the desired spectral result as both the HOMO and LUMO are displaced in the same direction. Furthermore, the HOMO position cannot be varied freely as the redox potential of the dye must be maintained sufficiently positive to ascertain rapid regeneration of the dye by electron donation from iodide following charge injection into the TiO_2. Therefore, the optimum Ru polypyridyl complexes should exhibit excited state oxidation potential of at least – 0.9 V vs. SCE, in order to inject electrons efficiently into the TiO_2 conduction band [30]. The ground state oxidation potential should be about 0.5 V vs. SCE in order to be regenerated rapidly via electron donation from the electrolyte (iodide/triiodide redox system or a hole conductor). A significant decrease in electron injection efficiencies will occur if the excited and ground state redox potentials are lower than these values. To trap solar radiation efficiently in the visible and the near-infrared region of the solar spectrum requires engineering of sensitizers at a molecular level [30].

1.5.1
Modulation of Sensitizer's Spectral Response

Ruthenium complexes show strong visible bands due to charge transfer transition from metal t_{2g} (HOMO) orbitals to π^* (LUMO) orbitals of the ligand. From spectroscopic and electrochemical studies of polypyridyl complexes of Ru, it has been concluded that the oxidation and reduction potentials are the best indicators of the energy levels of the HOMO and LUMO [31]. The energy gap between the metal t_{2g} orbitals and π^* orbitals can be reduced either by raising the energy of the t_{2g} or by decreasing the energy of the π^* orbitals with donor acceptor ligands, respectively (Fig. 4). In the following sections we will discuss the ways to tune HOMO and LUMO energy levels by introducing various ligands.
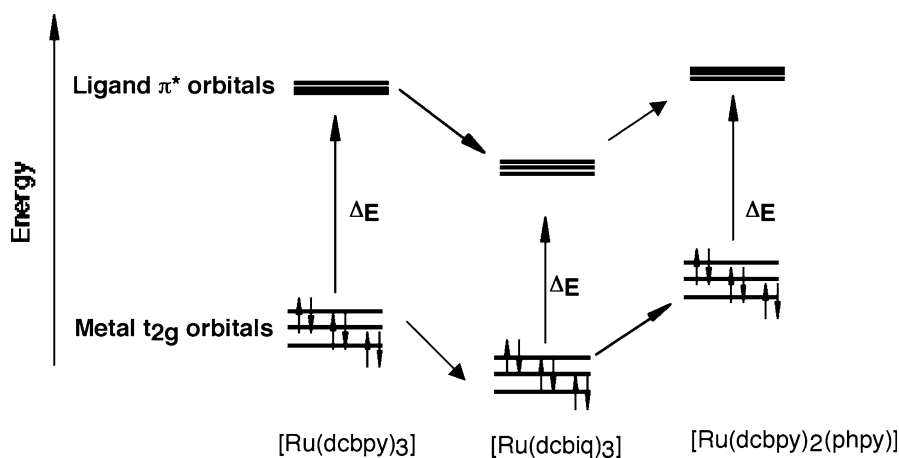

Fig. 4 Schematic representation of tuning the HOMO (t_{2g}) and LUMO (π^*) orbital energies

1.5.1.1
Spectral Tuning in "Push–Pull" Type of Complexes

The lowest energy MLCT transition of Ru polypyridyl complexes of the type tris-[Ru(4,4′-dicarboxy-2,2′-bipyridine)$_3$] (**1**), can be lowered so that it absorbs more in the red region of the visible spectrum by replacing one 4,4′-dicarboxy-2,2′-bipyridine (dcbpy) with two thiocyanate donor ligands [Ru(dcbpy)$_2$(NCS)$_2$] (**2**). In complex **2**, the two 4,4′-dicarboxylic acid 2,2′-bipyridine ligands pull while the two thiocyanate donor ligands push electrons. The oxidation potential of the complex **2** is 0.85 V vs. SCE, which is cathodically shifted significantly (0.65 V vs. SCE) compared to the homoleptic type of complex **1**, which shows Ru(III/II) couple at 1.5 V vs. SCE. Thus, the
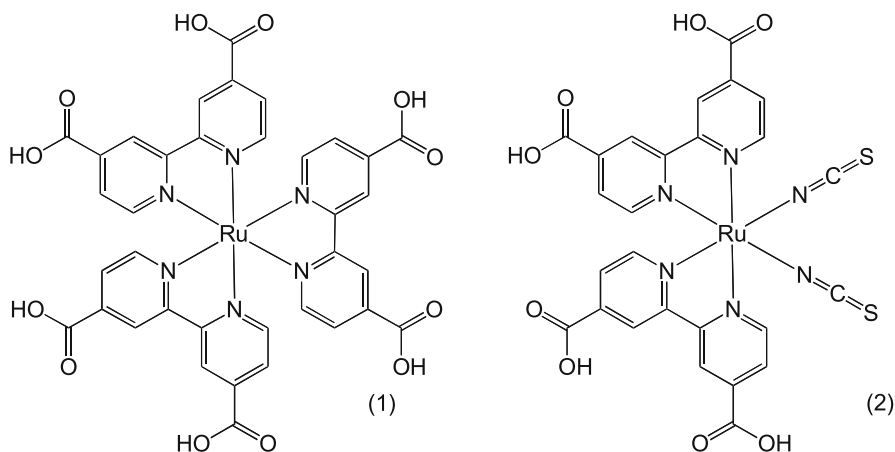
energy of the HOMO is varied 0.65 V, by replacing one 4,4′-dicarboxylic acid 2,2′-bipyridine with two thiocyanate ligands.

Figure 5 shows the absorption spectra of complexes **1** and **2**, which exhibit maxima at 465 nm, and 535 nm, respectively. It is interesting to note the magnitude of the spectral shift for the lowest energy charge transfer transition, i.e., ≈ 0.35 eV, and the shift in the oxidation potential, ≈ 0.65 eV. This clearly shows that the HOMO tuning is not all translated into the spectral shift of the complex. The apparent 0.3 eV difference is involved in raising the energy of the π^* orbitals of the pulling ligands caused by the pushing ligands [32]. In complex **2**, the purpose of incorporating carboxylic acid groups in the 4,4′-position of 2,2-bipyridine ligand is twofold: to graft the dye on
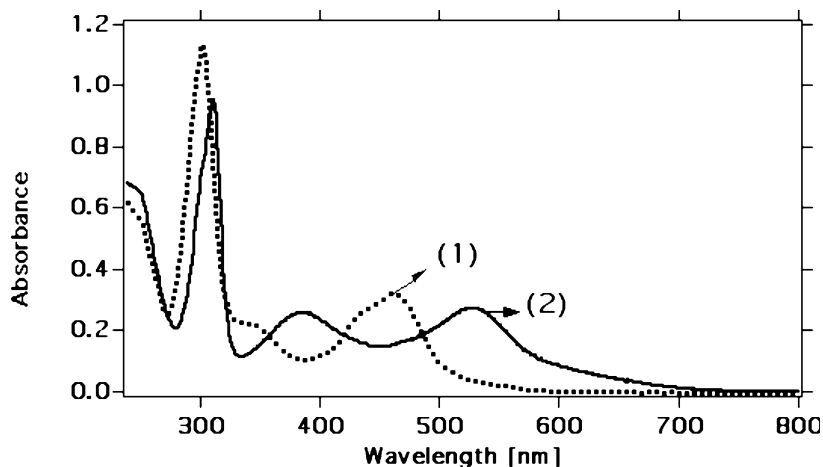

Fig. 5 Comparison of absorption spectra of complexes **1** and **2**

the semiconductor surface, and to provide intimate electronic coupling between its excited state wave-function and the conduction band manifold of the semiconductor. The role of the thiocyanato ligands is to tune the metal t_{2g} orbitals of Ru(II) and possibly to stabilize the hole that is being generated on the metal, after having injected an electron into the conduction band.

The other interesting class of compounds, which contains donor and acceptor groups in the same hybrid ligand such as 2,6-bis(1-methylbenzimidazol-2'-yl)-pyridine (3–7). The hybrid ligand in these complexes contains donor (benzimidazol-2'-yl) and acceptor groups and was further tuned by introducing different substituents on the benzimidazol-2'-yl group. The complexes containing these ligands show intense UV absorption bands at 362 and 346 nm due to intraligand π–π^* transition of 2,6-bis(1-methylbenzimidazol-2'-yl)-pyridine, which acts as a UV filter in dye-sensitized solar cells [33].
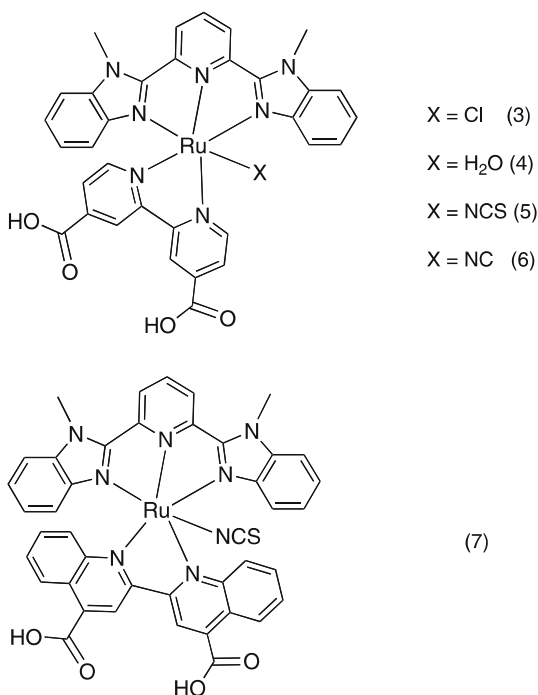
The MLCT bands of these complexes are broad and red-shifted by 140 nm, compared to the complex 1. The lowest-energy MLCT transitions within this series were shifted from 486 to 608 nm, and the HOMO level varied over an extent of 0.45 V vs SCE. The energy of the MLCT transition in these complexes decreases with the decrease in the π-acceptor strength of the ancillary ligand, i.e., CN^-, NCS^-, H_2O, or Cl^-. The red shift of the absorption maxima in complexes containing 4,4'-dicarboxy-2,2-biquinoline (dcbiq) (7) as

(8)   (9)
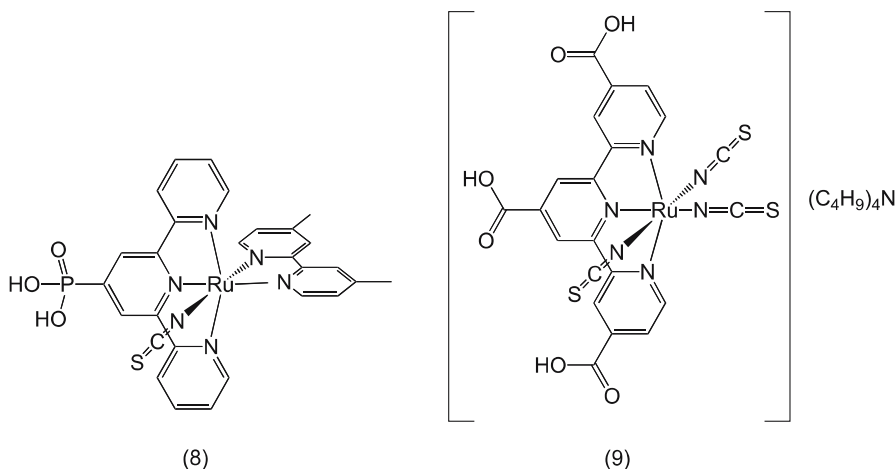
opposed to complex **5** (which contains dcbpy) is due to the low-lying π^* orbitals of dcbiq. The resonance Raman spectra of these complexes for excitation at 568 nm show predominantly bands associated with the dcbpy and dcbiq ligands, indicating that the lowest excited state is a metal-to-dcbpy or dcbiq ligand charge transfer state [34].

1.5.1.2
Influence of Nonchromophoric Ligands on MLCT Transitions

In this section we will compare the spectral response of the two complexes of the type [Ru(P-terpy)(Me$_2$bpy)(NCS)] (**8**), and ((C$_4$H$_9$)$_4$N)$_2$[RuL(NCS)$_3$] (**9**) (P-terpy = 4-phosphonato-2,2′:6′,2″-terpyridine, Me$_2$bpy = 4,4′-dimethyl-2,2′-bipyridine, L′ = 4,4′,4″-tricarboxy-2,2′:6′,2″-terpyridine), where the number of nonchromophoric ligands such as NCS$^-$ changed from one to three. The MLCT transition maxima of complexes **8** and **9** are at 500 and 620 nm, respectively. The 120-nm red shift of complex **9** compared to complex **8** is due to an increase in the energy of the metal t_{2g} orbitals caused by introducing nonchromophoric ligands. The electrochemical data are consistent with the above assignments [35, 36].

1.5.1.3
Geometrical Isomers

Isomerization is another approach for tuning the spectral properties of metal complexes [37–39]. The UV-Vis absorption spectrum of the *trans*-dichloro complex (**10**) in dimethylformamide (DMF) solution shows at least three MLCT absorption bands in the visible region at 690, 592, and 440 nm. On the other hand, the *cis*-dichloro complex (**11**) in DMF solution shows only

(10)   (11)   (12)
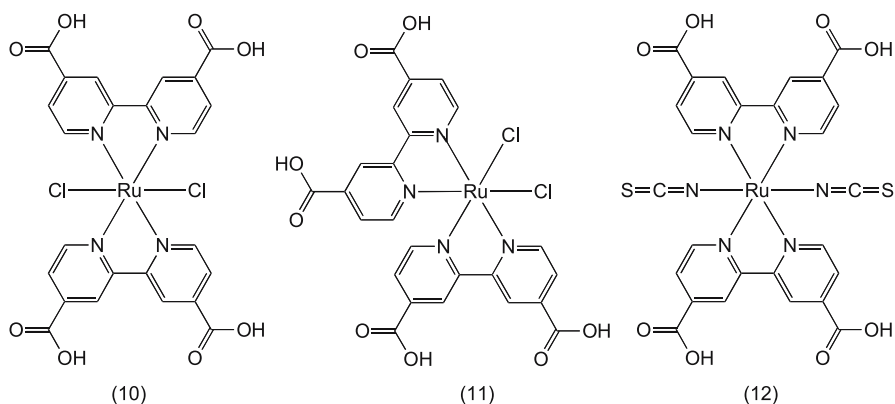
two distinct broad bands in the visible region at 590 and 434 nm, which were assigned to MLCT transitions. The lowest energy MLCT band in *trans*-dithiocyanate complex (**12**) is significantly red-shifted compared to the corresponding *cis*-complex (**2**) (Fig. 6). This red shift is due to stabilization of the LUMO of the dcbpy ligand in the *trans* species relative to the *cis* species. The red shift (108 nm) of the lowest energy MLCT absorption in the spectrum of the *trans*-dichloro complex compared to the spectrum of the *trans*-
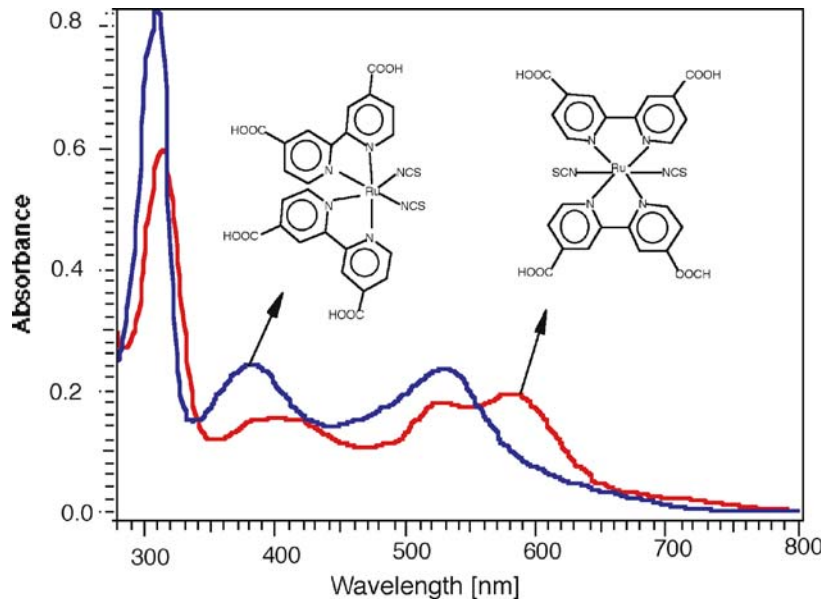

Fig. 6 UV-Vis absorption spectra of *cis*-, and *trans*-bis(4,4′-dicarboxy-2,2′-bipyridine) Ru(II)(NCS)₂ complexes

dithiocyanato is due to the strong σ donor property of the Cl$^-$ compared to the NCS$^-$ ligand. The chloride ligands cause destabilization of the metal t_{2g} orbitals, and raise them in energy relatively closer to the ligand π^* orbitals, resulting in a lower energy MLCT transition.

1.5.1.4
Hydrophobic Sensitizers

The other important aspect in dye-sensitized solar cells is water-induced desorption of the sensitizer from the TiO$_2$ surface. Extensive efforts have been made in our laboratory to overcome this problem by introducing hydrophobic properties in the ligands **13–17**. The absorption spectra of these complexes show broad features in the visible region and display maxima around 530 nm. The performance of these hydrophobic complexes as charge transfer photosensitizers in nanocrystalline TiO$_2$-based solar cells shows excellent stability towards water-induced desorption [36].

(13)	R =	CH$_3$
(14)	R =	C$_6$H$_{13}$
(15)	R =	C$_9$H$_{19}$
(16)	R =	C$_{13}$H$_{27}$
(17)	R =	C$_{18}$H$_{37}$
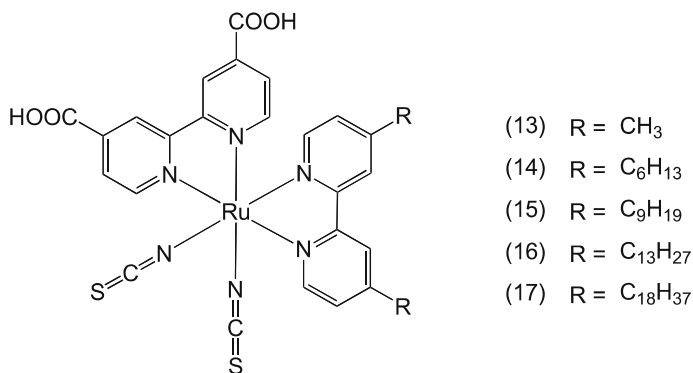
The rate of electron transport in dye-sensitized solar cells is a major element of the overall efficiency of the cells. The injected electrons into the conduction band, from optically excited dye, can traverse the TiO$_2$ network and can be collected at the transparent conducting glass or can react either with oxidized dye molecule or with the oxidized redox couple (recombination). The reaction of injected electrons into the conduction band with the oxidized redox mediator gives undesirable dark currents, reducing significantly the charge-collection efficiency, and thereby decreasing the total efficiency of the cell (Fig. 7).

Several groups have tried to reduce the recombination reaction by using sophisticated device architecture such as composite metal oxides as the semiconductor with different band gaps [40, 41]. Gregg et al. have examined surface passivation by deposition of insulating polymers [42]. We have studied the influence of spacer units between the dye and the TiO$_2$ surface with little
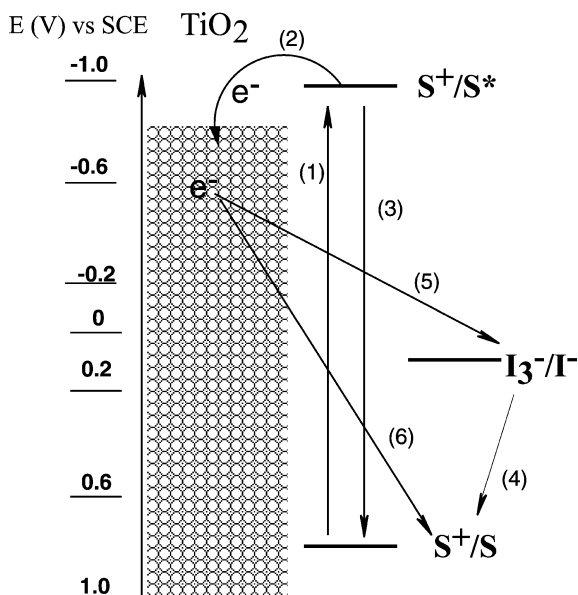
Fig. 7 Illustration of the interfacial charge transfer processes in nanocrystalline dye-sensitized solar cell. $S/S^+/S^*$ represents the sensitizer in the ground, oxidized and excited state, respectively. Visible light absorption by the sensitizer (1) leads to an excited state, followed by electron injection (2) into the conduction band of TiO_2. The oxidized sensitizer (3) gets reduced by I^-/I_3^- redox couple (4). The injected electrons into the conduction band may react either with the oxidized redox couple (5) or with oxidized dye molecule (6)

success [30]. Nevertheless, by using TiO_2 films containing hydrophobic sensitizers that contain long aliphatic chains (**13–17**) the recombination reaction was suppressed considerably [43, 44]. The most likely explanation for the reduced dark current is that the long chains of the sensitizer interact laterally to form an aliphatic network, as shown in Fig. 8, thereby preventing triiodide from reaching the TiO_2 surface.

1.5.1.5
High Molar Extinction Coefficient Sensitizers

Complex **2** has become a paradigm in the area of dye-sensitized nanocrystalline TiO_2 films [45]. In spite of this, the main drawback of this sensitizer is the lack of absorption in the red region of the visible spectrum and also a relatively low molar extinction coefficient. Therefore, a new series of high molar extinction coefficient sensitizers (**18–20**) featuring alkyloxy groups has been synthesized and utilized in dye-sensitized solar cells. The purpose of the 4,4′-di-(2-(3,6-dimethoxyphenyl)ethenyl)-2,2′-bipyridine ligand, which contains extended π-conjugation with substituted methoxy groups, is to enhance
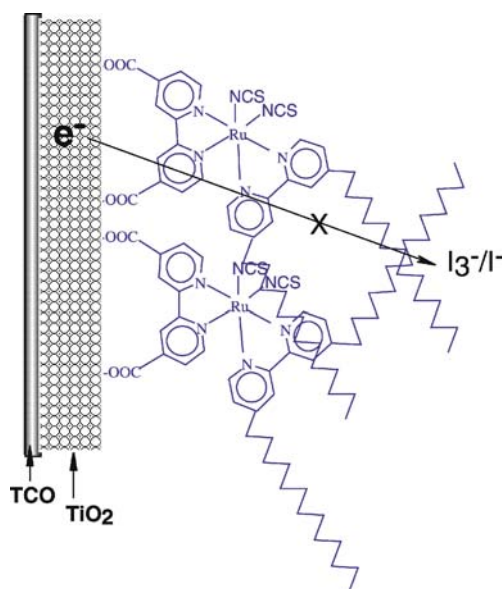
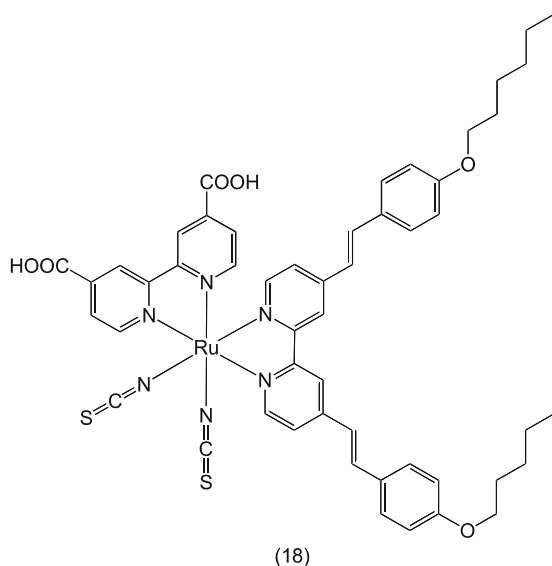**Fig. 8** Pictorial representation of the blocking of the oxidized redox couple I_3^- from reaching the surface of TiO_2 for conduction band electrons using hydrophobic sensitizers, which form an aliphatic network

(18)

the molar extinction coefficient of the sensitizers, and furthermore to provide directionality in the excited state by fine tuning the LUMO level of the ligand with the electron-donating alkoxy groups.

(19)

(20)
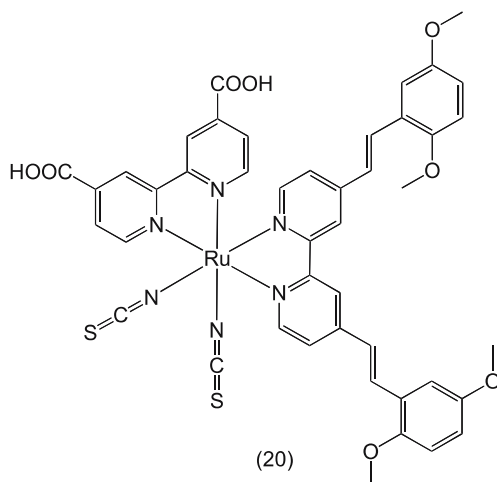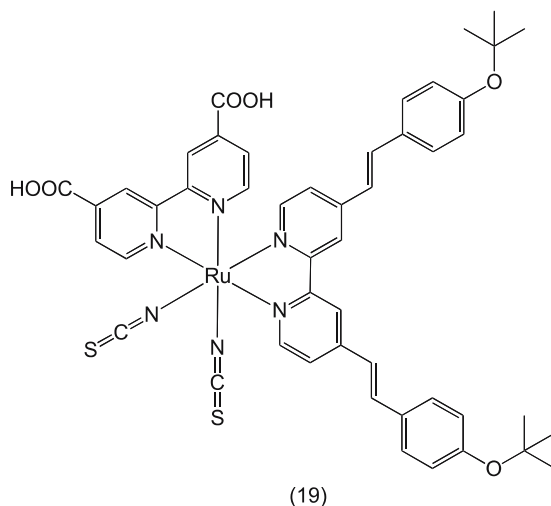
The absorption spectra of complexes **18–20** are dominated by the MLCT transitions in the visible region, and the lowest allowed MLCT bands appearing at 400 and 545 nm. The molar extinction coefficients of these bands are close to 35 000 and 19 000 $M^{-1}cm^{-1}$, respectively, which are significantly higher than those of the standard sensitizer *cis*-dithiocyanatobis(4,4′-dicarboxy-2,2′-bipyridine)Ru(II), (**2**) (Fig. 9).

Figure 10 shows an INDO/S and DFT (density functional theory) study of the electronic and optical properties of complexes **18–20**. The theoretical data point to the top three frontier-filled orbitals having essentially Ru 4d (t_{2g} in octahedral group) character with sizable contribution coming from the NCS ligand orbitals [46]. Most critically, the calculations reveal that for

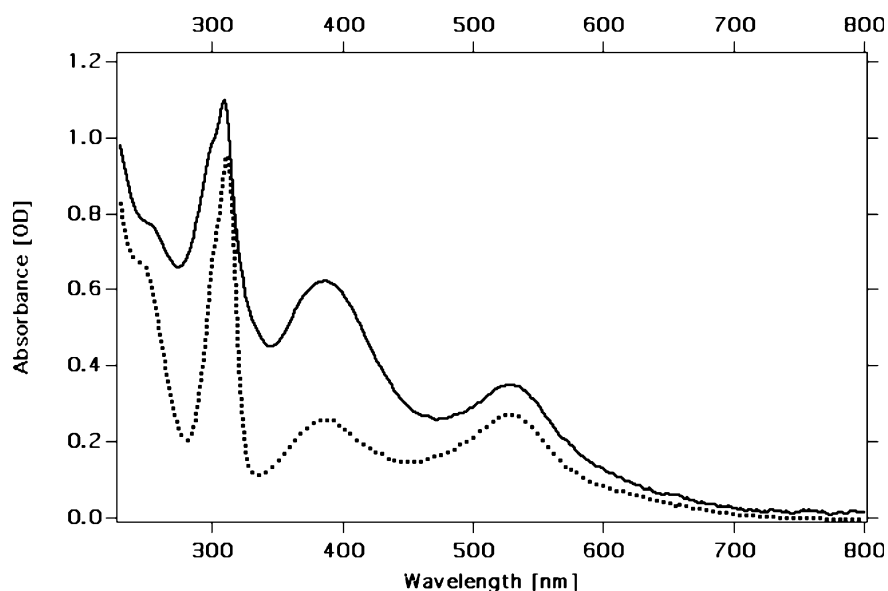**Fig. 9** Comparison of absorption spectra of complexes **2** and **20** in ethanol
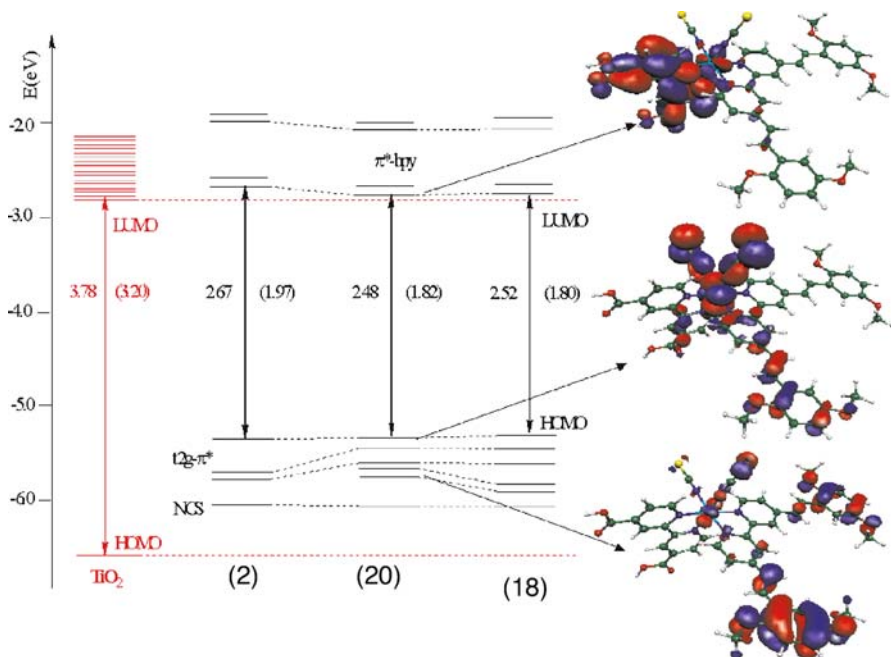

Fig. 10 Molecular orbital energy diagram of complexes **2**, **18**, and **20** compared to that of a TiO$_2$ nanoparticle model. HOMO–LUMO gaps (eV) and lowest TDDFT excitation energies (eV, data in parenthesis) are reported together with isodensity plots of the HOMO-3, HOMO, and LUMO of complex **20**

the TiO_2-bound sensitizers **18–20**, excitation directs charge into the carboxyl-bipyridine ligand bound to the TiO_2 surface. The photovoltaic data of these sensitizers using an electrolyte containing 0.60 M butylmethylimidazolium iodide (BMII), 0.03 M I_2, 0.10 M guanidinium thiocyanate and 0.50 M *tert*-butylpyridine in a mixture of acetonitrile and valeronitrile (volume ratio: 85 : 15), exhibited a short circuit photocurrent density of 16.50 ± 0.2 mA cm^{-2}, with an open circuit voltage of 790 ± 30 mV and a fill factor of 0.72 ± 0.03. This corresponds to an overall conversion efficiency of 9.6% under standard AM 1.5 sunlight and demonstrates stable performance under light and heat soaking at 80 °C [47].

1.5.1.6
Sensitizers Containing Functionalized Hybrid Tetradentate Ligands

The main advantage of *trans* complexes **10** and **12** discussed above is their panchromatic response, but the drawback is thermal and photoinduced isomerization back to the *cis* configuration. In an effort to stabilize the *trans* configuration of an octahedral Ru complex and integrate the concepts of donor and acceptor in a single complex, Renouard et al. and Barolo et al. have developed functionalized hybrid tetradentate ligands and their Ru complexes (**21–24**) [48, 49]. In these complexes the donor units of the tetradentate ligand (benzimidazole in **21–22** and tert-butylpyridine in **23–24**) tune the metal t_{2g} orbital energies, and the acceptor units (methoxycarbonyl) tune the π^* molecular orbitals. The application of a tetradentate ligand will inhibit the *trans* to *cis* isomerization process. The axial coordination sites are used to further fine-tune the spectral and redox properties and to stabilize the hole that is being generated on the metal during electron injection into the conduction band.

The *trans*-dichloro and dithiocyanate complexes **21–24** show MLCT transitions in the entire visible and near IR region. The lowest energy MLCT transition band of the *trans*-dichloro complexes **21** is around 700 nm in DMF

(21)   (22)
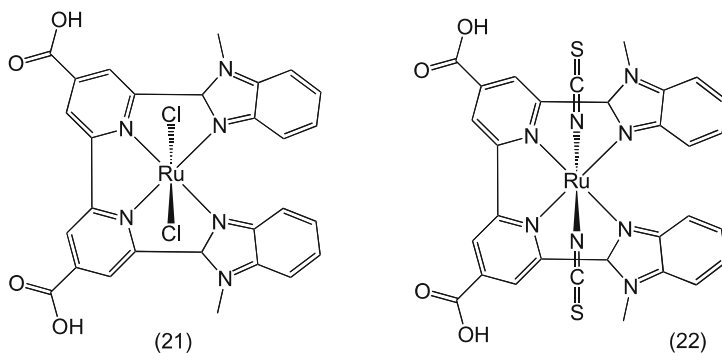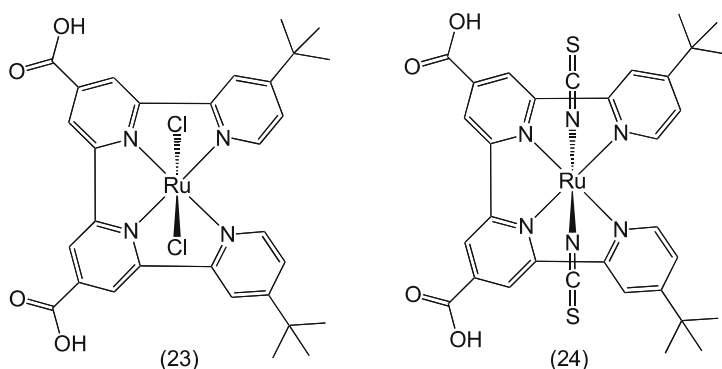
solution and they show weak and broad emission signals with onset above 950 nm [48]. The absorption spectra of the *trans*-dithiocyanate complex **24** are blue-shifted with respect to its *trans*-dichloro analogues due to the weak σ donor property of the NCS$^-$ compared to the Cl$^-$, which is consistent with the electrochemical data of these complexes. A comparison of absorption spectra of complex **24** and complex **2** is shown in Fig. 11. The spectra are dominated by features in the entire visible region at 382(sh), 465, 515, and 637 nm, which are assigned as MLCT. The lowest energy MLCT band in complex **24** is red-shifted by 107 nm when compared to the standard sensitizer **2** (see Fig. 11).
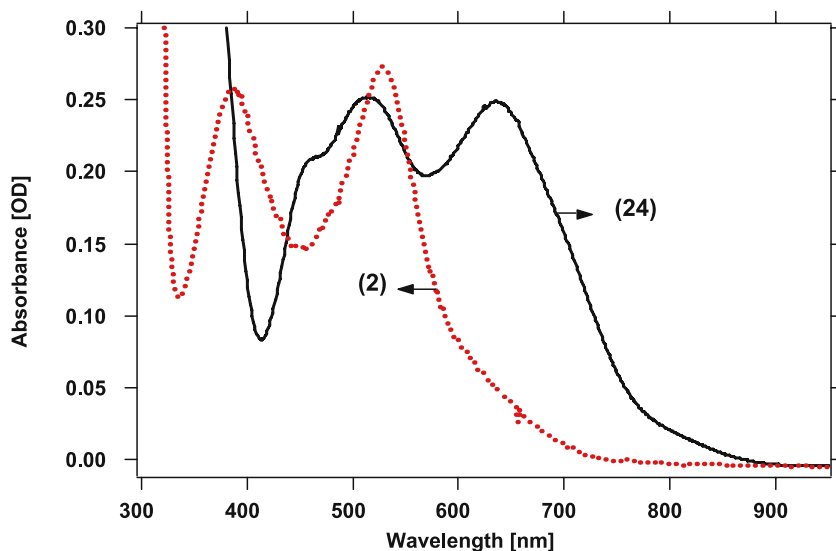

Fig. 11 UV-Vis absorption spectra of complexes **24** and **2** (concentration 3.5×10^{-5} M) and N719 (concentration 2.0×10^{-5} M) measured in ethanol solution and their chemical structures

Figure 12 shows the cyclic voltammogram of complex **24**. The Ru(III/II) redox potentials of the thiocyanate complexes were more positive (by $\approx$ 350 mV) than their corresponding dichloro complexes and show quasi-reversible behavior [49]. This is in good agreement with the ligand electro-chemical parameter scale, according to which the thiocyanate Ru(III/II) wave should be ~ 340 mV more positive than that of the dichloro species [50]. The i_{ox}/i_{red} peak current is substantially greater than unity due to the oxidation of the thiocyanate ligand subsequent to the oxidation of the Ru(II) center. At negative potentials an irreversible reduction wave (labeled as III in Fig. 12) appeared at -1.39 V, which is due to reduction of protons on the carboxylic acid of 4,4$'''$-di-(*tert*-butyl)-2,2$'$:6,2$''$:6$''$,2$'''$-quaterpyridine-4$'$,4$''$-dicarboxylic acid [51]. The quasi-reversible wave at $E_{1/2} = -1.93$ V vs. Fc is assigned to the reduction of the 4,4$'''$-di-(*tert*-butyl)-2,2$'$:6,2$''$:6$''$,2$'''$-quaterpyridine-4$'$,4$''$-
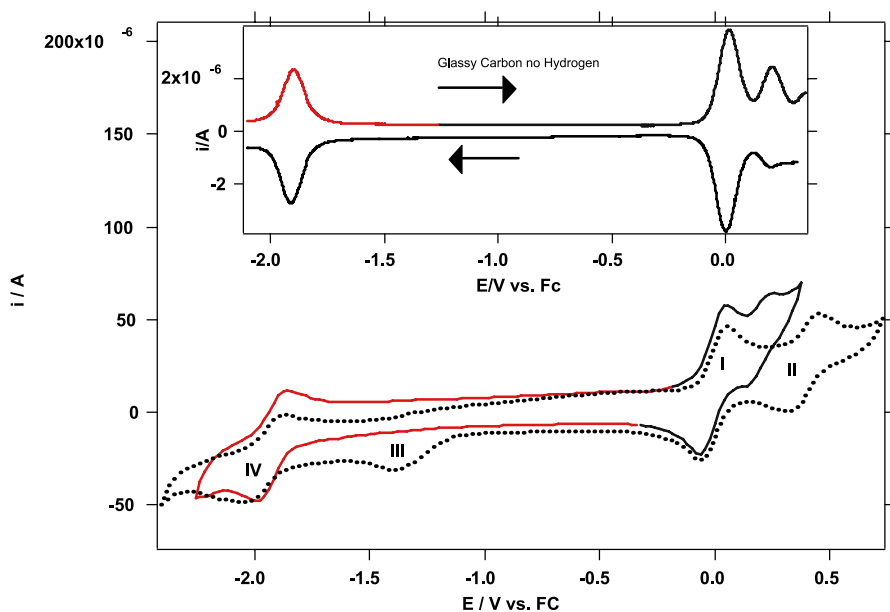
Fig. 12 Cyclic voltammogram of complex **24** in protonated (*black line*) and deprotonated state (*red line*) measured in DMF solution containing 0.1 M TBA(PF$_6$) using a glassy carbon electrode with scan rate of 500 mV s^{-1}. The redox couple labeled *I* is due to fer-rocenium/ferrocene, which is used as an internal standard; *II* is Ru(III/II); *III* is proton reduction and *IV* is due to ligand reduction. *Insert* shows differential pulse voltammo-gram of complex **24** in the deprotonated state, measured in DMF solution containing 0.1 M TBA(PF$_6$) using a glassy carbon electrode with ferrocene as an internal reference. The direction of the change in electrode polarization is shown with *arrows* (from negative to positive (*red curve*) and positive to negative potentials (*black curve*)), with a step po-tential of 10 mV, modulation amplitude 25 mV, modulation time 0.05 s, and interval time 0.5 s

(2)   (24)
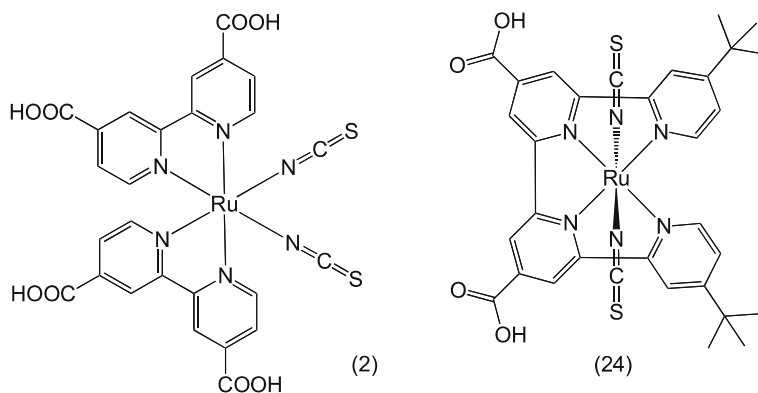
dicarboxylic acid ligand (wave IV). Upon deprotonation of the complex by treating with tetrabutylammonium hydroxide or by electrochemical reduction of protons to hydrogen the irreversible couple (wave III) disappeared, accompanied by a quasi-reversible wave IV. The ligand-based reduction couple in the deprotonated form compares well with that of the protonated form. Therefore, the origin of the irreversible peak is explicitly attributed to reduction of protons to hydrogen.

The electronic spectra of **24** were calculated by DFT/TDDFT and compared with the experimental data. Geometry optimization of **24** produced a structure with C_2 point group symmetry [49]. The schematic isodensity plots of the frontier orbitals of **24** are shown in Fig. 13. The seven HOMOs of **24** show contributions from both the Ru center and the SCN ligands in variable percentages. In particular, the first two almost degenerate HOMOs, lying within 0.04 eV, are antibonding combinations of the Ru d_{xz} and d_{yz} orbitals with the SCN π orbitals, while HOMO-2 and HOMO-4, lying 0.51 and 0.93 eV below the HOMO, respectively, are non-bonding d_{xy}-SCN π combinations. HOMO-3, lying 0.80 eV below the HOMO, is a pure SCN π orbital, while the almost degenerate HOMO-5/HOMO-6 represent the bonding counterpart of the d_{xz}/d_{yz}(Ru)-π(SCN) orbitals and lie 1.32 eV below the HOMO. It is interesting to compare the electronic structure of complex **2** with that of complex **24**. Both complexes show seven highest HOMOs of mixed Ru–SCN character.

The seven LUMOs of complex **24** are π^* combinations localized on the quaterpyridine ligand, while the LUMO+7 and LUMO+8 have d_{z2}(Ru) and d_{x2-y2}(Ru) character, respectively, and lie ca. 0.8 eV above LUMO+6. The LUMO/LUMO+2 are mainly localized on the portion of the ligand bearing the COOH groups. In particular, the LUMO is localized on the pyridines bearing the carboxylic groups and on the carbon–carbon bond connecting them. The LUMO+1/LUMO+2, lying 0.55 eV above the LUMO, also have amplitudes on the carbon–carbon bonds connecting the pyridines. The LUMO+3 and LUMO+6, lying 1.27 and 2.06 eV above the LUMO, are completely delocal-
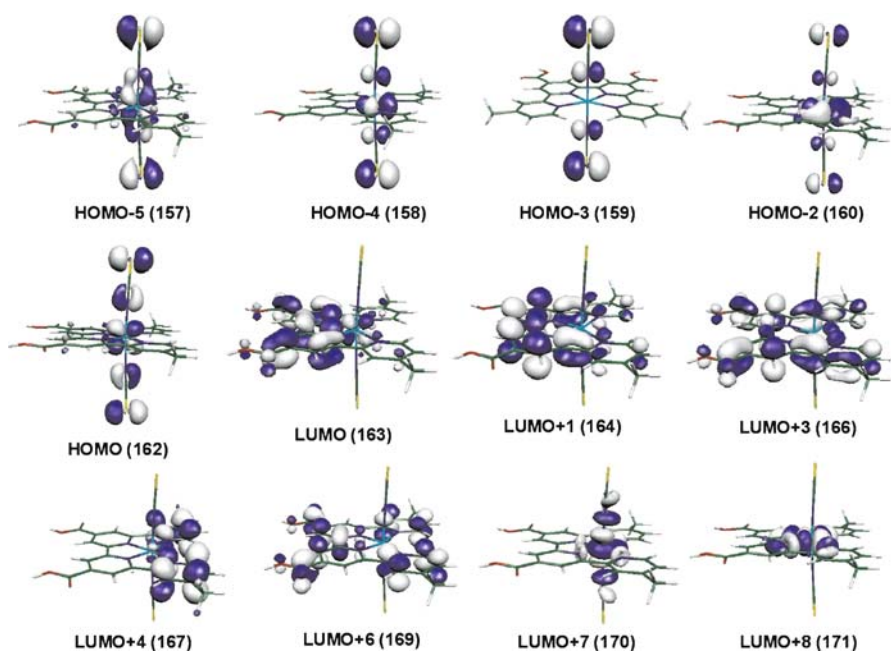
Fig. 13 Isodensity plots of the frontier orbitals of complex **24**

ized over the tetradentate ligand; the LUMO+4/LUMO+5, found 1.62 eV above the LUMO, are localized on the two pyridine bearing the alkyl-substituted groups. LUMO, LUMO+3, and LUMO+6 show contributions from the COOH groups.

1.6
Surface Chelation of Polypyridyl Complexes onto the TiO₂ Oxide Surface

The functional groups serve to anchor the dye onto the TiO_2 films. The grafting of polypyridyl complexes onto the oxide surface, which allows for electronic communication between the complex and the substrate, is an important feature in dye-sensitized solar cells. Several Ru complexes containing substituted groups such as carboxylic acid, hydroxamic acid dihydroxy, and phosphonic acid on pyridine ligands are described [52–61]. These functional moieties serve as an anchoring group to immobilize the complex on the nanocrystalline TiO_2 films. The immobilized sensitizer absorbs a photon to produce an excited state, which transfers an electron onto the TiO_2 conduction band. To achieve high quantum yields for electron injection, the dye needs to be in intimate contact with the semiconductor surface to produce close overlap of the ligand π^* orbitals with the titanium 3d orbitals. The values reached with Ru complexes that have carboxylic acid and phospho-

nic acid groups are close to 100%. A quantum yield near unity implies that the electron injection is at least a hundred times more rapid than the natural decay time of the sensitizer, which is in the nanosecond range.

The interaction between the adsorbed sensitizer and the semiconductor surface has been addressed using resonance Raman and FT-IR spectroscopy. The carboxylic acid functional group could adsorb on the surface in a unidentate, bidentate, or bridging fashion. Yanagida et al. concluded that the sensitizer *cis*-dithiocyanato bis(2,2′-bipyridine-4,4′-dicarboxylate)Ru(II) (**2**) binds to the surface using ester-like chelating linkages [62]. Finnie et al. have reported that the sensitizer **2** anchors on the surface of TiO$_2$ as a bidentate or bridging mode using two carboxylate groups per dye [63]. However, Fillinger
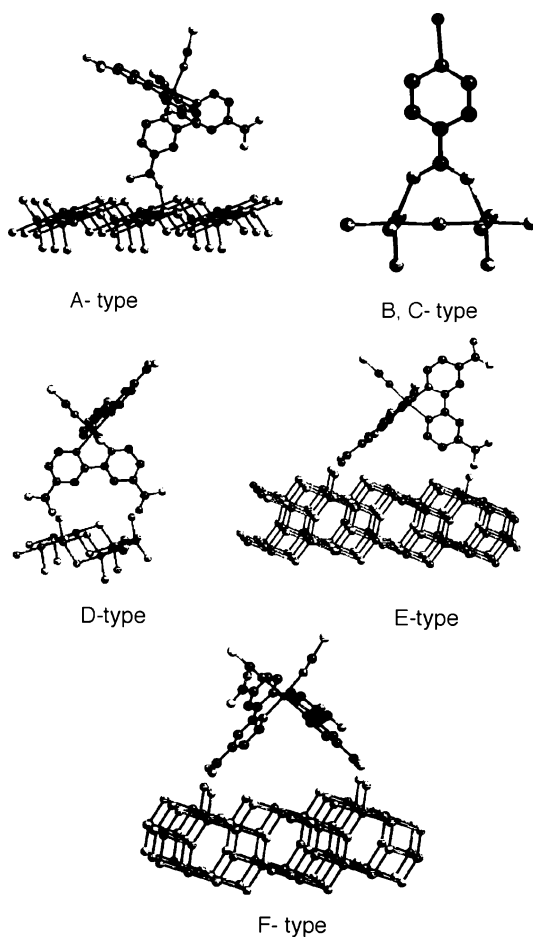

A- type

B, C- type

D-type

E-type

F- type

Fig. 14 Possible anchoring modes for sensitizer **2** using carboxylate functional group on TiO$_2$ surface

and Parkinson studied the adsorption behavior of the sensitizer **2** and found that the initial binding involves one carboxylate, with subsequent additional binding of two or more carboxylate groups on the surface [64].

Shklover et al. have reported the crystal structure and molecular dynamics modeling of the sensitizer **2** with different anchoring types to the TiO_2 anatase surface [65]. In their modeling the initial attachment of the dye is a single bond A-type (Fig. 14). The main feature of this type of anchoring is the great rotational freedom of the molecule, which leads to immediate capture of another carboxylic group by a neighboring Ti atom, resulting in anchoring B- and C-type (Fig. 14). When the sensitizer **2** anchors onto the TiO_2 surface, using both carboxylic groups of the same bipyridyl ligand, this results in a two-bond anchoring of the D-type (Fig. 14). In E- and F-type configuration, attachment occurs via two of its four carboxylic groups. The carboxylic group either bridges two adjacent rows of titanium ions through bidentate coordination or interact with surface hydroxyl groups through hydrogen bonds. The two remaining carboxylic groups remain in the protonated state. Thermodynamically the bonding geometry of the E- and F-type are most favorable. The ATR-FTIR data of the sensitizer **2** and its different protonated forms adsorbed on TiO_2 are consistent with the anchoring of F-type where the sensitizer adsorbs on the surface using two carboxylic groups as a bridging bidentate fashion, which are *trans* to the NCS ligands [66].

1.6.1
Acid–Base Equilibria of *cis*-Dithiocyanato Bis(2,2′-bipyridine-4,4′-dicarboxylate)Ru(II) Complex(2)

Understanding of the binding nature of sensitizers onto the TiO_2 surface requires detailed knowledge of the pK_a's of the sensitizer. Here we discuss pK_a's of the sensitizer **2** and its implications for the adsorption studies. The ground state pK_a values of **2** were determined from the relationship between the change in the optical density or the peak maximum with the pH for a given wavelength [26]. The plot of λ_{max} change vs. pH for **2** shows the expected sigmoidal shape, with the pH at the inflection point giving two ground state pKa values at 3 and 1.5 ± 0.1. In complex **2** there are two 4,4′-dicarboxy-2,2′-bipyridine ligands that could give four separate acid–base equilibria, if the dissociation is stepwise. On the other hand, if the dissociations were simultaneous one would expect one equilibrium constant. The two separate equilibria in complex **2**, suggests that the pyridyl subunits are not equivalent [66]. The stronger Lewis basicity of the thiocyanato compared to the bipyridine ligand increases the pK_a value of the pyridine carboxylic acid, which is opposite to its own position in the octahedral complex, shifting its pK_a to a higher value than that of the second pyridine carboxylic acid, to which it is connected.

1.7
Photovoltaic Properties

The best photovoltaic performance, both in terms of conversion yield and long term stability, has so far been achieved with polypyridyl complexes of Ru in which two 2,2′-bipyridyl-4,4′-dicarboxylic acid and thiocyanate ligands have been used. Thus, the Ru complex *cis*-RuL$_2$(NCS)$_2$ (**1**), known as N3 dye, has become the paradigm of heterogeneous charge transfer sensitizer for mesoporous solar cells [19] The fully protonated N3 has absorption maxima at 535 and 400 nm, the extinction coefficients being 1.45 and 1.41×10^4 M^{-1} cm^{-1}, respectively. The complex emits at 750 nm with a lifetime of 60 ns. The optical transition has MLCT character: excitation of the dye involves transfer of an electron from the metal to the π^* orbital of the surface anchoring carboxylated bipyridyl ligand. From here it is released within femto- to picoseconds into the conduction band of TiO$_2$, generating electric charges with near-unit quantum yield.

1.7.1
Effect of Protons Carried by the Sensitizer on the Performance

In order to obtain high overall light to electric power conversion efficiencies, optimization of the short circuit photocurrent (i_{sc}) and open circuit potential (V_{oc}) of the solar cell is essential. The conduction band of the TiO$_2$ is known to have a Nernstian dependence on pH [55, 67]. The fully protonated sensitizer **2**, upon adsorption transfers most of its protons to the TiO$_2$ surface, charging it positively. The electric field associated with the surface dipole generated in this fashion enhances the adsorption of the anionic Ru complex and assists electron injection from the excited state of the sensitizer into the titania conduction band, favoring high photocurrents (18–19 mA cm^{-2}). However, the open-circuit potential (0.65 V) is lower due to the positive shift of the conduction band edge induced by the surface protonation.

On the other hand, the sensitizer **25**, which carries no protons, shows high open-circuit potential compared to complex **2**, due to the relative negative shift of the conduction band edge induced by the adsorption of the anionic complex. However, as a consequence the short circuit photocurrent is lower. Thus, there should be an optimal degree of protonation of the sensitizer in order to maximize the product of short circuit photocurrent and open circuit potential, which along with the fill factor determines the power conversion efficiency of the cell.

The performance of the three sensitizers **2**, **25** and **26**, which contain different degrees of protonation, were studied on nanocrystalline TiO$_2$ electrodes [26]. Figure 16 shows the photocurrent action spectra obtained with a monolayer of these complexes coated on TiO$_2$ films.

(25)

(26)
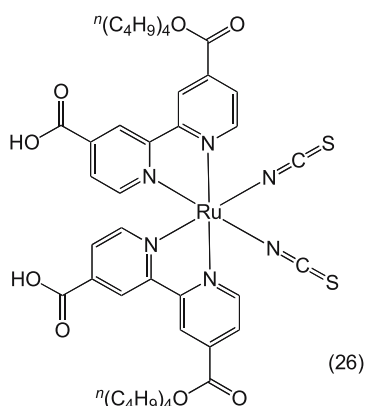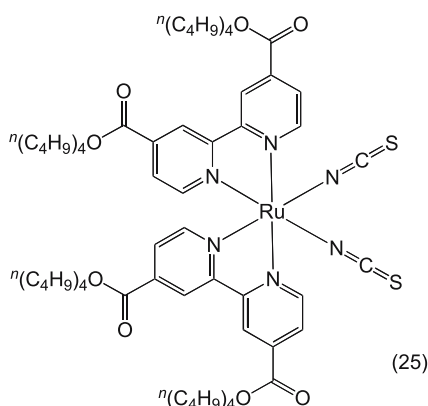
The incident monochromatic photon-to-current conversion efficiency (IPCE) is plotted as a function of excitation wavelength. The IPCE value in the plateau region is 80% for complex **2**, while for complex **25** it is only about 66%. In the red region, the difference is even more pronounced. Thus, at 700 nm the IPCE value is twice as high for the fully protonated complex **2** as compared to the deprotonated complex **25**. As a consequence, the short circuit photocurrent is 18–19 mA cm^{-2} for complex **2**, while it is only about 12–13 mA cm^{-2} for complex **25**. However, there is a trade-off in photovoltage, which is 0.9 V for complex **25**, as compared to 0.65 V for complex **2**. Nevertheless, this is insufficient to compensate for the current loss. Hence, the
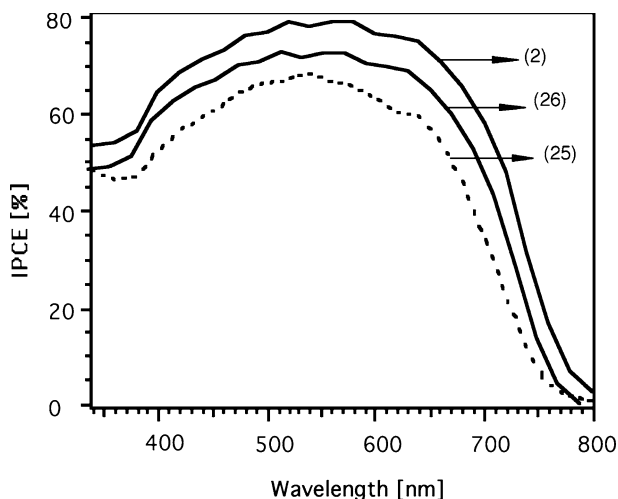

Fig. 15 Photocurrent action spectra of nanocrystalline TiO$_2$ films sensitized by complexes **2**, **25**, and **26**. The incident photon to current conversion efficiency is plotted as a function of wavelength

photovoltaic performance of complex **26** carrying two protons is superior to that of compounds **2** and **25** that contain four or no protons, respectively. The doubly protonated form of the complex is therefore preferred over the other two sensitizers for sensitization of nanocrystalline TiO_2 films.

The solar to electric power conversion efficiency of dye-sensitized solar cells of laboratory scale (0.158 cm^2), validated by an accredited photovoltaic calibration laboratory, has reached 11.1% under standard reporting conditions, i.e., air mass 1.5 global sunlight at 1000 W m^{-2} intensity and 298 K temperature, rendering it a credible alternative to conventional p-n junction photovoltaic devices [68]. Photovoltaic performance data obtained with a sandwich cell under illumination by simulated AM 1.5 solar light using complex **26** are shown in Fig. 16. At 1 sun the **26**-sensitized solar cell exhibited 17.73 ± 0.5 mA current, 846 mV potential, and a fill factor of 0.75 yielding an overall conversion efficiency of 11.18%.
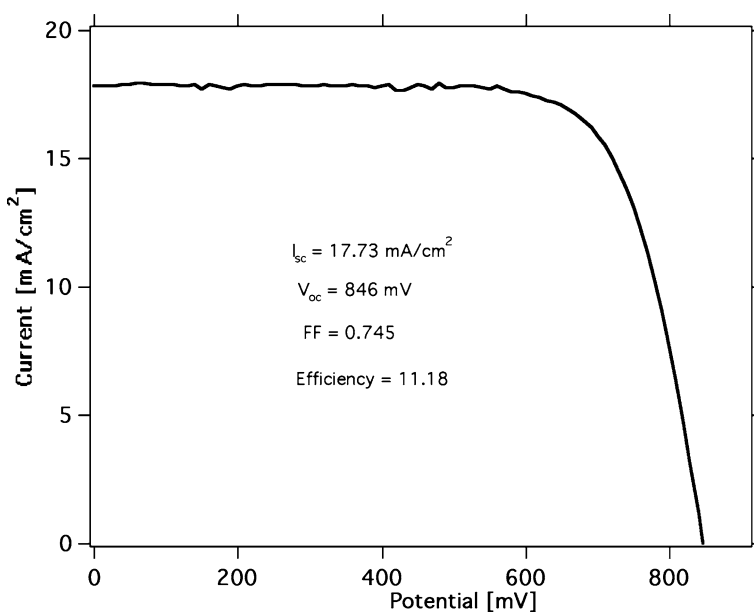
Fig. 16 Photocurrent–voltage curve of a solar cell based on complex **26**. The cell was equipped with an anti-reflective coating. The conversion efficiency in full AM 1.5 sunlight illumination (100 mW cm^{-2}) is 11.18%. The cell is masked with black plastic to avoid the diffusive light leaving an active cell area of 0.158 cm^2

1.7.2
Comparison of IPCE Obtained with Various Sensitizers

Figure 17 shows the photocurrent action spectrum of a cell containing various sensitizers. The broad feature covers the entire visible spectrum and
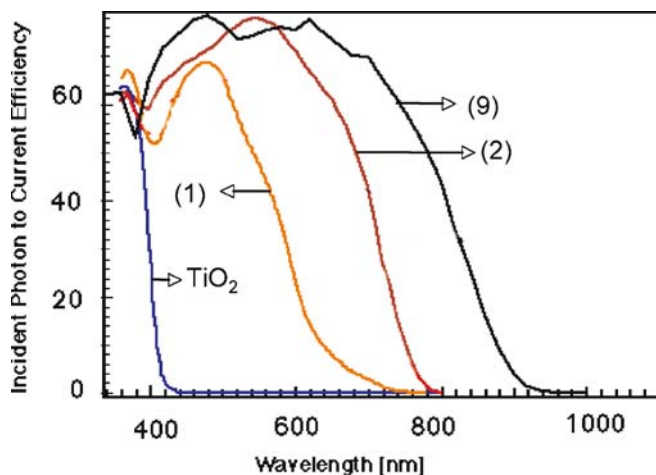
Fig. 17 Photocurrent action spectra of bare nanocrystalline TiO$_2$ film, and the sensitizers **1**, **2**, and **9** adsorbed on TiO$_2$ films. The incident photon to current conversion efficiency is plotted as a function of wavelength

extends into the near IR region up to 920 nm for complex **9**. The incident photon-to-current conversion efficiency value in the plateau region was about 80% for complex **9**. Taking the light losses in the conducting glass into account, the efficiency of electric current generation is practically 95% over a broad wavelength. The overlap integral of the absorption spectrum with the standard global AM 1.5 solar emission spectrum for complex **9** yields a photocurrent density of 20.5 mA cm^{-2}. The open circuit potential is 720 mV and the fill factor is 0.7, resulting in a total power conversion efficiency of 10.5%. These results were confirmed at the National Renewable Energy Laboratory (NREL), Golden, Colorado, USA (Fig. 18). The complexes [RuL$_3$] (**1**) and [RuL$_2$(NCS)$_2$] (**2**) under similar conditions show an IPCE value of 70–80% in the plateau region. Though the IPCE values are comparable with that of **9**, the total integrated current decreased significantly due to increasing blue shift of the spectral response from **9** to **2** to **1**.

1.7.3
Solid State Dye-Sensitized Solar Cells

Research on the solid state dye-sensitized solar cells (DSC) has gained considerable momentum recently as this embodiment is attractive for realizing flexible photovoltaic cells in a roll-to-roll production. The *spiro*-OMeTAD has been the most successful p-type organic conductor (hole transport material) employed. Its work function is about 4.9 eV and the hole mobility 2×10^{-4} cm^2 s^{-1}. A schematic diagram of the solid sate DSC with the structure of this hole conductor is shown in Fig. 19. Reported first in 1998, the con-

EPFL (Switzerland) nano-crystal dye sensitized cell

Sample: PL0710/2
Oct 30, 1998 10:41 AM
ASTM E 892-87 Global

Temperature = 25.0°C
Area = 0.1863 cm^2
Irradiance: 1000.0 Wm^{-2}

NREL X-25 IV System

V_{oc} = 0.7210 V
I_{max} = 3.552 mA
J_{sc} = 20.53 mAcm^{-2}
Fill Factor = 70.41%

V_{max} = 0.5465 V
I_{sc} = 3.824 mA
P_{max} = 1.941 mW
Efficiency = 10.4%
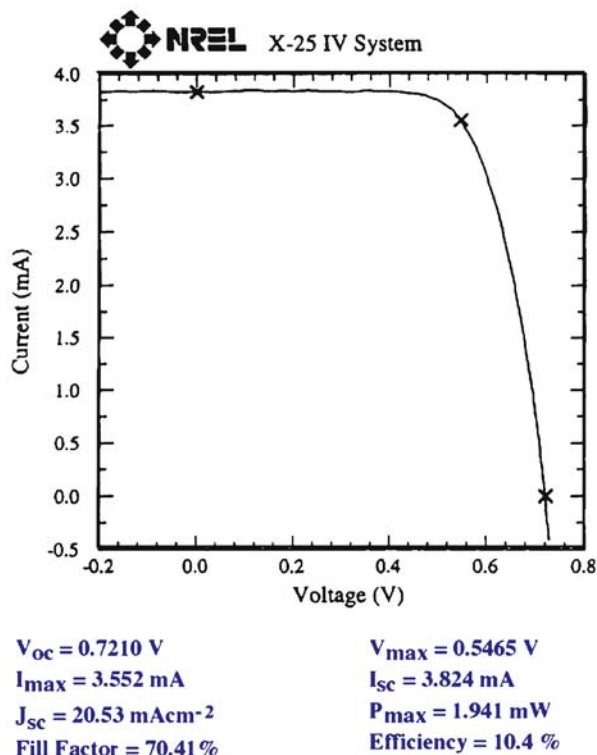
Fig. 18 Photocurrent–voltage characteristics of complex **9** measured at the National Renewable Energy Laboratory

version yields have increased dramatically over the last few years, i.e., from a fraction of a percent to over 4% [43, 69]. The main drawback of these cells has been fast interfacial electron-hole recombination, reducing the diffusion length of the conduction band electrons to a few microns as compared to 20–100 microns for the electrolyte-based DSC. As a consequence, the film thickness employed in these cells is restricted to only 2 microns, which is insufficient to harvest the sunlight by the adsorbed sensitizer, thus reducing the resultant photocurrent. The dye monolayer itself blocks this back reaction because it is electrically insulating [70]. Hence, current efforts are being directed towards molecular engineering of the interface to improve the compactness and order of monolayer and prevent in this fashion the charge carriers from recombining.
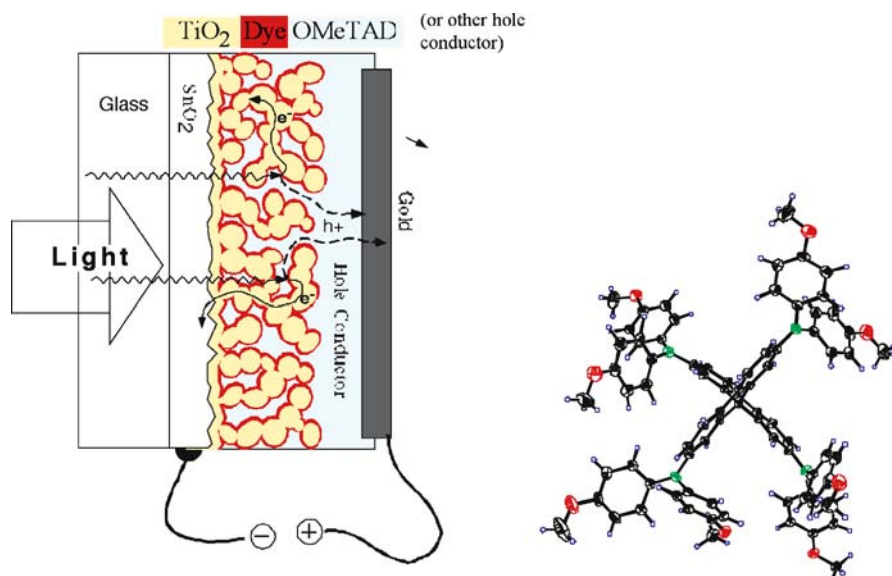
Fig. 19 Cross-sectional view of a solid state dye-sensitized photovoltaic cell using the hole conductor spiro-OMeTAD, whose structure is indicated on the *right*

Another difficulty encountered has been the filling of the porous network with the hole conductor. This impediment may be overcome by developing oxide films having regular mesoporous channels aligned in a perpendicular direction to the current collector. On the other hand, the V_{OC} values obtained with solid state DSCs are high, reaching nearly 1 V, due to a better match of the hole conductor work function than that of the electrolyte with the redox potential of the sensitizer. The future of these solid hole conductor systems thus looks bright if the recombination and pore filling problems can be addressed.

1.8
Stability

In contrast to amorphous silicon, which suffers from degradation due to the well-known Stabler–Wronski effect, the intrinsic stability of the DSC has been confirmed by extensive accelerated light soaking tests carried out over the last decade. One major issue that has been settled during this period is that the sensitizers employed in the current dye-sensitized solar cell embodiments can sustain 20 years of outdoor service without significant degradation. However, as new and more advanced dye structures emerge, and in order to avoid repeating these lengthy tests every time the sensitizer is modified, kinetic criteria have been elaborated to allow prediction of long-term performance.

Figure 20 illustrates the catalytic cycle that the sensitizer undergoes during cell operation. Critical for stability are side reactions that occur from the excited state (S^*) or the oxidized state (S^+) of the dye. These reactions compete with electron injection from the excited dye into the conduction band of the mesoscopic oxide and with the regeneration of the sensitizer. These destructive channels are assumed to follow first or pseudo-first order kinetics and are assigned the rate constants k_1 and k_2. Introducing the two branching ratios $P_1 = k_{inj}/(k_1 + k_{inj})$ and $P_2 = k_{reg}/(k_2 + k_{reg})$, where k_{inj} and k_{reg} are the first order or pseudo-first order rate constants for the injection and regeneration process, respectively, the fraction of the sensitizer molecules that survives one cycle is given by the product $P_1 \times P_2$. A simple calculation [71] shows that the sum of the branching ratios for the two bleeding channels should not exceed 1×10^{-8} in order for the lifetime of the sensitizer to reach a lifetime of at least 20 years. The turnover frequency of the dye, averaged over seasons and day/night time, is about $0.16\ \text{s}^{-1}$.
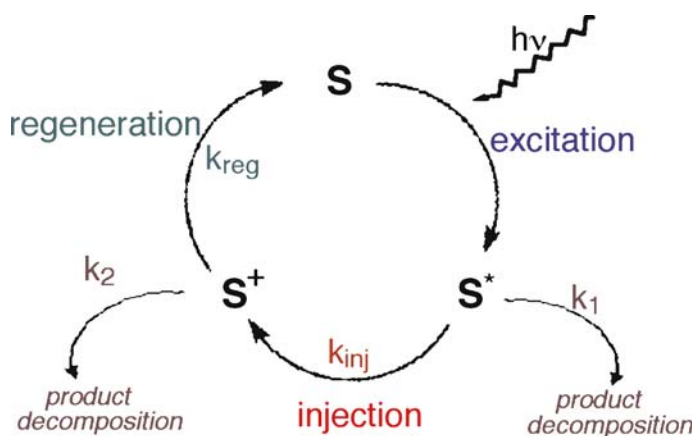
Fig. 20 Catalytic cycle of the sensitizer during cell operation

For most of the common sensitizers, the rate constant for electron injection from the excited state to the conduction band of the TiO_2 particles is in the femtosecond range. Assuming $k_{inj} = 1 \times 10^{13}\ \text{s}^{-1}$, any destructive side reaction should have $k_1 < 10^5\ \text{s}^{-1}$. Ru sensitizers of the type **26** and **18** readily satisfy this condition as the decomposition from the excited state level occurs at a much lower rate than the $10^5\ \text{s}^{-1}$ limit. Precise kinetic information has also been gathered for the second destructive channel involving the oxidized state of the sensitizer, the key parameter being the ratio k_2/k_{reg} of the rate constants for the degradation of the oxidized form of the sensitizer and its regeneration. The S^+ state of the sensitizer can be readily produced by chemical or electrochemical oxidation and its lifetime determined independently

by absorption spectroscopy. A typical value of k_2 is around 10^{-4} s^{-1} while the regeneration rate constant is at least in the 10^5 s^{-1} range. Hence the branching ratio is well below the limit of 10^{-8}, which can be tolerated to achieve the 100 million turnovers and a 20 year lifetime for the sensitizer.

Many long-term tests have been performed with the N3-type Ru complexes, confirming the extraordinary stability of these charge transfer sensitizers. For example, a European consortium supported by the Joule program [72] has confirmed cell photocurrent stability over 8500 h of light soaking at 2.5 suns, corresponding to ca. 56 million turnovers of the dye without any significant degradation. These results corroborate the projections from the kinetic considerations made above. A more difficult task has been to reach stability under prolonged stress at higher temperatures, i.e., 80–85 °C. The recent introduction of hydrophobic sensitizers has been particularly rewarding in this regard by allowing the dye-sensitized solar cell to meet, for the first time, the specifications laid out for outdoor applications of silicon photovoltaic cells [73]. In addition, these dyes show enhanced extinction coefficients due to the extension of the π-conjugation on one of the bipy ligands by styrene moieties. Taking advantage of these properties and using a novel robust electrolyte formulation, a $\geq$ 8% efficiency dye-sensitized solar cell has been realized showing strikingly stable performance under both prolonged thermal stress and light soaking [47]

While impressive progress has been made in the development of stable, non-volatile electrolyte formulations, the conversion yields obtained with these systems are presently in the 7–10% range, i.e., below the 11.1% reached with volatile solvents. Future research efforts will be dedicated to bridge the performance gap between these systems. The focus will be on hole conductors and solvent-free electrolytes such as ionic liquids. The latter are a particularly attractive choice for the first commercial modules, due to their high stability, negligible vapor pressure and excellent compatibility with the environment.

1.9
Pilot Production of Modules, Outdoor Field Tests and Commercial DSC Development

Figure 21 shows two prototypes of the monolithic Z-type interconnected modules, fabricated by Aisin Seiki in Japan. Note that carbon is used as a back contact to cut cost. Field tests of such modules already started several years ago and the results of these tests revealed advantages of the DSC with regards to silicon panels under realistic outdoor conditions. Thus, for equal rating under standard test conditions the DSC modules produced 20–30% more energy under real outdoor conditions than the polycrystalline silicon (pc-Si) modules. A photograph of the test station comparing the two types of photovoltaic technologies is shown in Fig. 22. The superior performance of the DSC can be ascribed to the following factors:
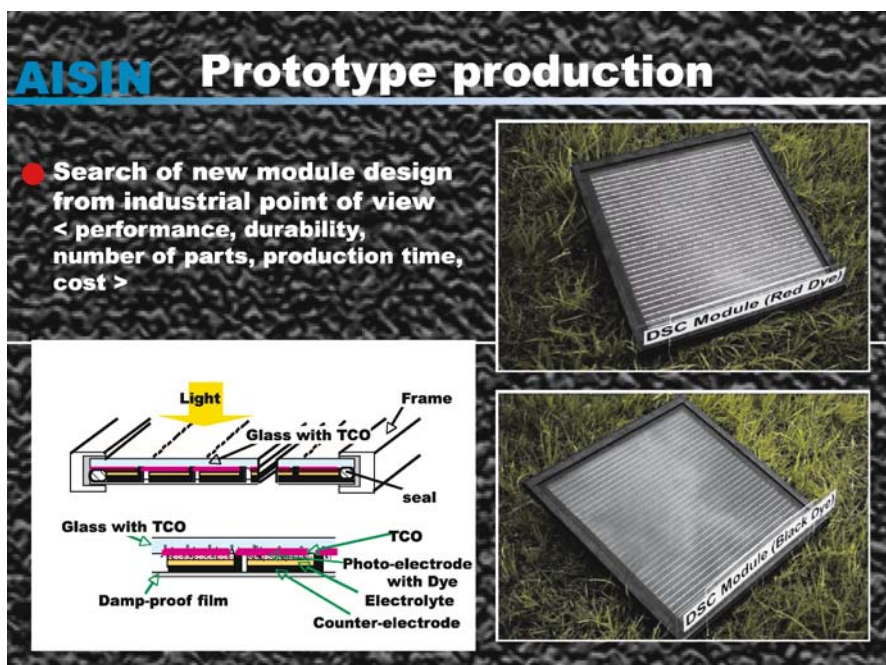
Fig. 21 Production of DSC prototypes by Aisin Seiki in Japan. Note the monolithic design of the photovoltaic modules and the use of carbon as interconnect and counter electrode material

- The DSC efficiency is practically independent of temperature in the range 25–65 °C while that of mono- and pc-Si declines by ca. 20% over the same range
- Outdoor measurements indicate that the DSC exhibits lower sensitivity to light capture as a function of the incident angle of the radiation, although this needs to be further assessed
- The DSC shows higher conversion efficiency than pc-Si in diffuse light or cloudy conditions

While it is up to the commercial supplier to set the final price for such modules it is clear that the DSC shares the cost advantage of all thin film devices. In addition, it uses only cheap and readily available materials. Finally, in contrast to amorphous silicon and CIGS cells the DSC avoids high vacuum production steps that are very cost intensive. Given these additional advantages at comparable conversion efficiency, module costs below 1 € are realistic targets even for production plants having well below gigawatt capacity. The DSC has thus become a viable contender for large-scale future solar energy conversion systems on the bases of cost, efficiency, stability, and availability as well as environmental compatibility.

Fig. 22 Outdoor field tests of DSC modules in Kariya City Japan at lat. 35°10′N, Azimuthal angle 0°, facing due south, tilted at 30°. Note the pc-Si modules in the *second row*

Fig. 23 The Toyota "Dream House" featuring DSC panels made by Aisin Seiki

DSC panels have also been installed in the walls of the Toyota "Dream House" (http://www.toyota.co.jp/jp/news/04/Dec/nt04_1204.html) shown in Fig. 23, offering a building-integrated source of solar power to the inhabitants. Very recently the British company G24I has announced the building of the first 20 MW DSC manufacturing plant in Wales (http://www.G24I.com).

1.9.1
Outlook

Using a principle derived from natural photosynthesis, mesoscopic injection solar cells and in particular the DSC have become a credible alternative to solid-state p-n junction devices. Conversion efficiencies over 11% and 15% have already been obtained with single junction and tandem cells, respectively, on the laboratory scale, but there is ample room for further amelioration. Future research will focus on improving the J_{SC} by extending the light response of the sensitizers in the near IR spectral region. Substantial gains in the V_{oc} are expected from introducing ordered oxide mesostructures and controlling the interfacial charge recombination by judicious engineering on the molecular level. Hybrid cells based on inorganic and organic hole conductors are an attractive option in particular for the flexible DSC embodiment. Nanostructured devices using purely inorganic components will be developed as well. The mesoscopic cells are well suited for a whole realm of applications ranging from the low power market to large-scale applications. Their excellent performance in diffuse light gives them a competitive edge over silicon in providing electric power for stand-alone electronic equipment both indoor and outdoor. Application of the DSC in building-integrated photovoltaics has already started and will become a fertile field of future commercial development. Almost 100 years ago, at the 1912 IUPAC conference in Washington, the famous Italian photochemist Professor Giacomo Ciamician from the University of Bologna predicted that mankind will unravel the secrets of photosynthesis and apply the principles used by plants to harvest solar energy in glass buildings. His visionary thoughts appear now close to becoming a reality.

2
Iridium Complexes as Triplet Emitters in Organic Light-Emitting Diodes

2.1
Introduction

Iridium(III) cyclometalated complexes are attracting widespread interest because of their unique photophysical properties and applications in organic light-emitting diodes (OLEDs). Several groups have used extensively neu-

tral Ir cyclometalated complexes in OLEDs and obtained up to 19% external quantum efficiencies, which require a complicated multilayered structure for charge injection, transport, and light emission [74–77]. An attractive alternative to the OLEDs is the light-emitting electrochemical cell (LEC) [78–82], which is particularly promising for large-area lighting applications. In these cells the use of ionic complexes facilitates electronic charge injection into the light-emitting film [78, 83, 84]. The main requirements for OLEDs and LECs are that the phosphorescent emitter should have sharp colors in the red, green and blue region, and exhibit very high phosphorescent quantum yields. Tuning phosphorescence wavelength, and enhancing phosphorescent quantum yields in these complexes in a predictable way is a daunting task, which of course is attractive for both fundamental research and practical applications [77, 85–89].

A strategy to tune the emission color in Ir(III) complexes relies on the selective HOMO stabilization and/or LUMO destabilization of the complex. Mixed ligand Ir complexes with C^N cyclometalating ligands, are particularly appealing in this respect, since the two types of ligands can be almost independently functionalized to obtain the desired color tuning [90]. In particular, electron-withdrawing substituents on the C^N ligands decrease the donation to the metal and therefore stabilize the metal-based HOMO. Electron-releasing substituents on the C^N ligand, lead, on the other hand, to destabilization of the ligand-based LUMO, ultimately leading to increased HOMO–LUMO gaps and emission energies. Much less clear are the factors that determine the emission quantum yields in mixed ligand complexes and on which parameters to act in order to increase them. It is indeed generally assumed that emission quantum yields should increase with increasing emission energy, due to the increase of the radiative rate constant and decrease of the non-radiative rate constants. These follow, respectively, the Einstein law of spontaneous emission [91] and the so-called energy gap law [92], even though exceptions to these rules are quite common.

2.2
Photophysical Properties

The photophysics of polypyridyl complexes of Ir can be understood with the aid of an energy level diagram, as shown in Fig. 24. In these complexes there are three possible types of excited states: (a) metal-centered (MC) excited states, which are due to promotion of an electron from t_{2g} to e_g orbitals; (b) ligand-centered (LC) states that are $\pi–\pi^*$ transitions; (c) MLCT states. An electronic transition from metal t_{2g} orbitals to empty ligand orbitals without spin change is allowed, which is called singlet–singlet absorption. The allowed transitions are identified by large extinction coefficients. The transitions with spin change are called singlet–triplet absorption, which are forbidden and associated with small extinction coefficients. However, the ex-
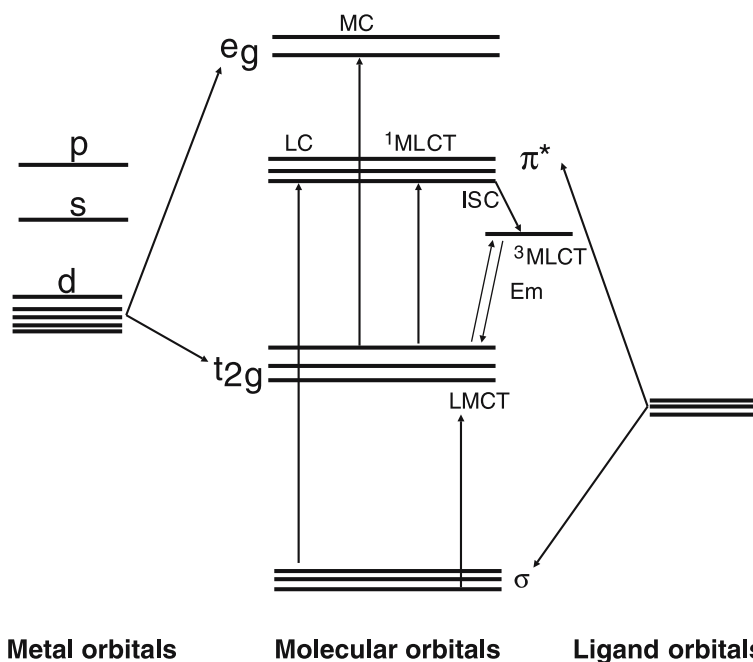
Fig. 24 Schematic and simplified molecular orbital diagram for an octahedral d^6 metal complex involving 2-phenylpyridine (C_3 symmetry)-type ligands in which various possible transitions are indicated

cited singlet state may be involved in spin flip, which is called intersystem crossing (ISC), resulting in an excited triplet state. The radiative process of a singlet and triplet excited state to a singlet ground state are termed fluorescence and phosphorescence, respectively. The excited singlet states associated with LC $\pi-\pi^*$ and MLCT transition can undergo ISC into the triplet state efficiently in Ir complexes due to spin-orbit coupling, resulting in enhanced phosphorescence quantum yields. For the cyclometalated Ir complexes, the wave function of the excited triplet state, responsible for phosphorescence, is principally expressed as a combination of the LC and the MLCT excited triplet state. However, not all the complexes are highly luminescent because of the different deactivation pathways.

2.3
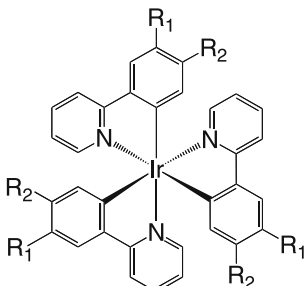## Tuning of Phosphorescence Colors in Neutral Iridium Complexes

Neutral Ir complexes were obtained by an orthometalation reaction with ligands that contain a benzene ring attached to a functional group containing a donor atom such as 2-phenylpyridine (ppy) and benzo[h]-quinoline (bzq) [93]. The coordination of ppy and bzq ligands to metal is analogous to

that found in 2,2′-bipyridine except that nitrogen is replaced by carbon anion [94]. In a typical example, three ppy ligands coordinate around Ir(III) resulting in a neutral complex, in which the phenyl group carries a formal negative charge due to loss of proton and subsequent orthometalation to Ir metal. The HOMO in tris-phenylpyridine Ir(III) [Ir(ppy)$_3$] is principally composed of orbitals of the phenyl ring and the metal d orbitals. The pyridine is formally neutral and is the major contributor to the LUMO in the [Ir(ppy)$_3$] complex [95].

The absorption spectra of [Ir(ppy)$_3$] display strong ligand-to-ligand (LC, $\pi-\pi^*$) and MLCT transitions in the UV and the visible region, respectively. The MLCT transition bands are lower in energy than the LC $\pi-\pi^*$ transitions. The excited triplet state shows strong phosphorescence in the green region at around 515 nm, with an excited state lifetime of 2 μs [96].

In order to tune the phosphorescence color of [Ir(ppy)$_3$], Watts et al. synthesized several substituted ppy-based neutral Ir complexes [96–98]. Table 1 shows the list of complexes that show strong phosphorescence from a ^{3}MLCT excited state. The phosphorescence lifetime of these complexes is in the range of 2–3 μs in nitrogen-saturated acetonitrile at room temperature [97]. The photophysical and electrochemical data (see Table 1) demonstrate the influence of ligands bearing electron-withdrawing and the electron-donating

Table 1 Emission, lifetime, and electrochemical data of complexes 27–34
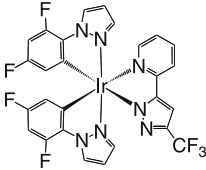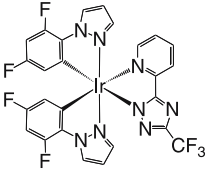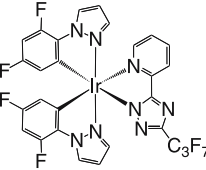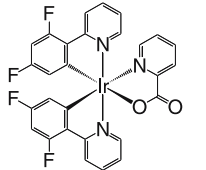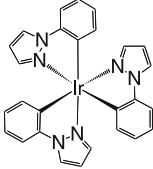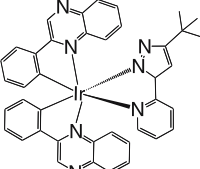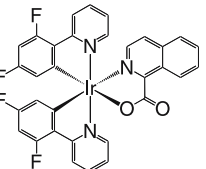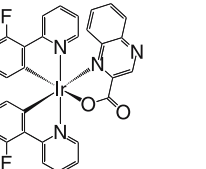
27 : R$_1$=H ; R$_2$=H
28 : R$_1$=H ; R$_2$=CH$_3$
29 : R$_1$=H ; R$_2$=C$_3$H$_7$
30 : R$_1$=H ; R$_2$=tBu
31 : R$_1$=H ; R$_2$=F
32: R$_1$=H ; R$_2$=CF$_3$
33 : R$_1$=H ; R$_2$=OCH$_3$
34: R$_1$=OCH$_3$; R$_2$=H

Complex	Emission λ_{max} (nm)	Lifetime τ (μs)	Potential vs. SCE $E_{1/2ox}$ (V)	Potential vs. Fc$^{+/0}$ (V)
27	494	1.9	0.77	0.37
28	493	1.9	0.70	0.30
29	496	1.9	0.67	0.27
30	497	2.0	0.66	0.26
31	468	2.0	0.97	0.57
32	494	2.2	1.08	0.68
33	481	2.2	0.75	0.35
34	539	2.9	0.55	0.15

substituents. It is interesting to note the difference between complexes **33** and **34** (Table 1), which is simply the effect of the position of electron-donating substitution on the phenyl ring. In complex **34** the electron-donating group is substituted at the 3-position of the phenyl ring. This destabilizes the HOMO by 0.2 V as compared to complex **33** in which the electron-donating group is substituted at 4-position. The HOMO of a ppy cyclometalated Ir complex is located primarily on the phenyl groups, therefore incorporation of an electron-donating substituent in the positions *para* to the Ir–carbon bond decreases the emission energy due to a *mesomeric* (oxygen lone pair donation to the aromatic π orbitals) effect. From the electrochemical data of the complexes shown in Table 1, it is evident that the less positive oxidation potential values result from ligands with electron-donating substituents, and more pos-

Table 2 Absorption, emission, and electrochemical properties of the iridium complexes **35–42**

Complex	Absorption λ_{max} (nm)	Emission[a] λ_{max} (nm)	Potential vs. Fc$^{+/0}$ $E_{1/2ox}$ (V)	$E_{1/2red}$ (V)	Lifetime (μs)
35	295, 349	455	0.98	− 2.72	0.040
36	300, 349	457	1.11	− 2.72	0.008
37	302, 348	455	1.11	− 2.53	0.009
38	–	468	1.00	− 1.9	–
39	321	444	0.41	− 3.20	–
40	359, 469	649	0.77	− 1.71	1.9
41		581		− 1.2	–
42		666	1.00	− 1.1	–

[a] Emission data were collected at 298 K

itive oxidation potential values result from ligands with electron-withdrawing substituents.

In these complexes the photophysical properties are very similar to the ppy-based Ir complexes because of substitution of electron-donating or electron-withdrawing groups on the phenyl ring. This is not surprising because the substitution of donor or acceptor groups tunes both the HOMO and LUMO levels of the metal complex to move in the same direction, leading to marginal changes in the photophysical properties.

In the mixed ligand complexes (**35–38** shown in Table 2) the HOMO levels have been stabilized significantly compared to the tris(ppy)Ir(III) complex, leading to blue shifts of the emission maxima, which is also apparent from the electrochemical data [87, 99]. On the other hand, the blue shift of the emission maxima in complex **39** is due to destabilization of LUMO of the 1-phenylpyrazolyl ligand. Several other groups have developed heteroleptic Ir complexes (see Table 2), in which the LUMO levels were stabilized (see Table 2 for $E_{\mathrm{red}}^{1/2}$ values of complexes **40–42**) compared to the tris(ppy)Ir(III) complex, leading to phosphorescent color maxima from green to red [89, 98–105]. Therefore, the compounds in Table 2 provide an exciting opportunity to tune the emission spectral properties from blue to red by simply selecting appropriate donor/acceptor ligands compared to the tris-homoleptic complexes of the type shown in Table 1.

2.4
Tuning of Phosphorescence Colors in Cationic Iridium Complexes

The tuning aspect of the MLCT transitions in cationic Ir complexes is illustrated by considering the following complexes: [Ir(2-phenylpyridine)$_2$(4, 4′-*tert*-butyl-2,2′-bipyridine)]PF$_6$ (**43**), [Ir(2,4-difluorophenylpyridine)$_2$(4,4′-dimethylamino-2,2′-bipyridine)]PF$_6$ (**44**), and [Ir(2-phenylpyridine)$_2$(4,4′-dimethylamino-2,2′-bipyridine)]PF$_6$ (**45**). These complexes were synthesized in a low-boiling solvent, dichloromethane, by reacting the corresponding dichloro-bridged Ir(III) dimer with 4,4′-*tert*-butyl-2,2′-bipyridine or 4,4′-dimethylamino-2,2′-bipyridine ligands (see Table 3) [106].

The cyclic voltammogram of complex **45** (Fig. 25) measured in acetonitrile containing 0.1 M tetrabutylammonium hexafluorophosphate with 100 mV s^{-1} scan rate shows a reversible wave at 0.72 V vs. Fc$^{+/0}$ due to oxidation of Ir(III) to Ir(IV), which is cathodically shifted by 210 mV compared to complex **43** due to the donor strength of 4,4′-dimethylamino-2,2′-bipyridine (Klein et al., unpublished data and [78, 106]). The three reversible reduction waves at – 2.17 and – 2.61 and – 2.87 V vs. Fc$^{+/0}$ (only two waves are shown in Fig. 25) are assigned to the reduction of 4,4′-dimethylamino-2,2′-bipyridine and the two ppy ligands, respectively. It is interesting to note that the ligand-based reduction potential of **45** is significantly shifted cathodically (390 mV) compared to complex **43**, demonstrating that the destabilization of

Table 3 Absorption, emission, and electrochemical properties of cationic iridium complexes **43**, **44**, and **45**

43   **44**   **45**

Complex	Absorption[a] λ_{max} (nm)	Emission[b] λ_{max} (nm)	Potential[c] $E_{1/2ox}$ (V)	vs. Fc$^{+/0}$ $E_{1/2red}$ (V)	Lifetime[d] (μs)
43	–	581[e]	0.88[e]	– 1.83[e]	0.557[e]
44	266 (8.27), 316 (2.89), 344 (2.20); 376 (1.45), 410 (0.41), 444 (0.14)	463, 493	1.0	– 2.13 – 2.49 – 2.77	4.11 ± 0.02
45	268 (5.62), 290 (3.49), 356 (0.95), 376 (0.85), 444 (0.19)	491, 520	0.72	– 2.17 – 2.61 – 2.87	2.43 ± 0.02

[a] Absorption data were measured in CH_2Cl_2 solution. Brackets contain values for molar extinction coefficient (ε) in 10^4 M^{-1} cm^{-1}

[b] Emission data were collected at 298 K by exciting at 380 nm

[c] Electrochemical measurements were carried out in acetonitrile solution and the potentials are V vs. ferrocenium/ferrocene (Fc$^{+/0}$)

[d] Lifetime data are collected in degassed solutions

[e] Data taken from [78]

the LUMO orbitals of 4,4′-dimethylamino-2,2′-bipyridine offsets more than the destabilization of the Ir HOMO orbitals caused by the electron-donating 4,4′-dimethylamino-2,2′-bipyridine ligand, ensuing an increase in the gap between the HOMO and the LUMO of **45** compared to the HOMO–LUMO gap of complex **43**.

The cyclic voltammogram of complex **44** shows a reversible couple at 1.0 V vs. Fc$^{+/0}$ due to oxidation of Ir(III) to Ir(IV), and two reversible reduction waves at – 2.13 and – 2.49 V vs. Fc$^{+/0}$ arising from the reduction of the 4,4′-dimethylamino-2,2′-bipyridine and 2-(2,4-difluorophenyl)pyridine ligand, respectively. The HOMO orbitals in **44** are stabilized upon insertion of fluoro substituents on the ppy ligands, thus ensuing an increase of the HOMO and LUMO gap of **44** compared to the HOMO and LUMO gap of **43** and **45** (Table 3) [106].

UV-Vis absorption spectra of the complexes **43**, **44**, and **45** in dichloromethane solution at 298 K display bands in the UV and the visible region
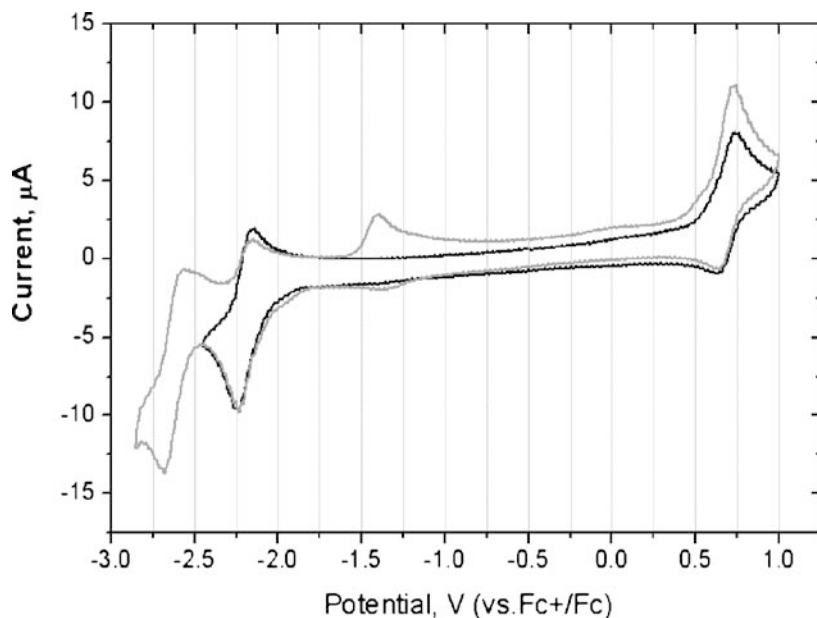
Fig. 25 Cyclic voltammogram of complex **45** measured in acetonitrile in the presence of 0.1 M tetrabutylammonium hexafluorophosphate as supporting electrolyte with 100 mV s^{-1} scan rate. The *black line* shows the scan between – 2.4 to 1 V, and the *gray line* between – 2.8 to 1 V. The observed irreversible new wave at around – 1.35 V is due to unknown product that is formed when scanning to more negative potential

due to intraligand (π–π^*) and MLCT transitions, respectively (Fig. 26 and Table 3) [107]. When excited at 298 K within the π–π^* or MLCT absorption bands, complex **44** shows emission maxima at 463 and 493 nm due to the 4,4′-

Fig. 26 Absorption and emission spectra of **44** (*solid line*) and **45** (*dashed line*) in dichloromethane solution at 298 K

dimethylamino-2,2′-bipyridine ligand that increases the gap between LUMO of 4,4′-dimethylamino-2,2′-bipyridine and HOMO of Ir, resulting in a blue shift of the emission maxima compared to **43** [78, 96].

It is worth noting that the argon-degassed dichloromethane solutions of **44** and **45** show bright luminescence in a lighted room, and display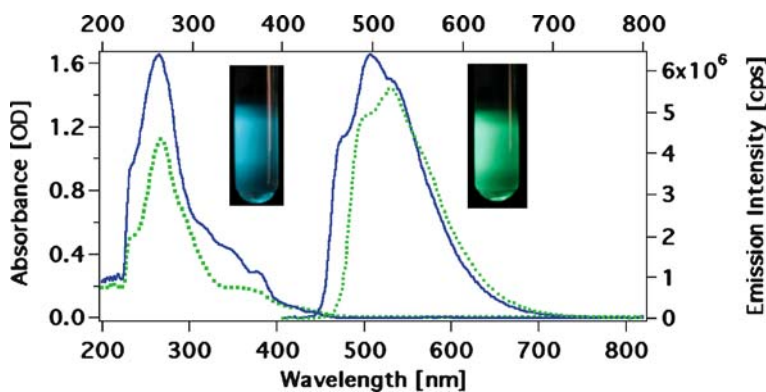 unusual phosphorescence quantum yields of $80 \pm 10\%$ in solution at room temperature. The emission spectral profile is independent of excitation wavelength, and the emission of **44** and **45** decayed as a single exponential with lifetimes of 2 and $4\,\mu s$ in dichloromethane solution, respectively [108].

The electronic structures of these complexes based on DFT calculations, together with plots of selected molecular orbitals are shown in Fig. 27. The HOMO in these complexes is an antibonding combination of $Ir(t_{2g})$ and $ppy(\pi)$ orbitals, and is calculated at -5.50 and $-5.66\,eV$ for **44** and **43**, respectively (De Angelis et al., unpublished data). The LUMO of both complexes is a π^* orbital localized on the 4,4′-dimethylamino-2,2′-bipyridine ligand and is calculated at -2.49 and $-2.3\,eV$ for **43** and **44**, respectively. At higher energy, the LUMO is followed by an almost degenerate couple of ppy π^* orbitals, whose energies approach that of the 4,4′-dimethylamino-2,2′-bipyridine π^* LUMO on going from **43**, **45** to **44**.
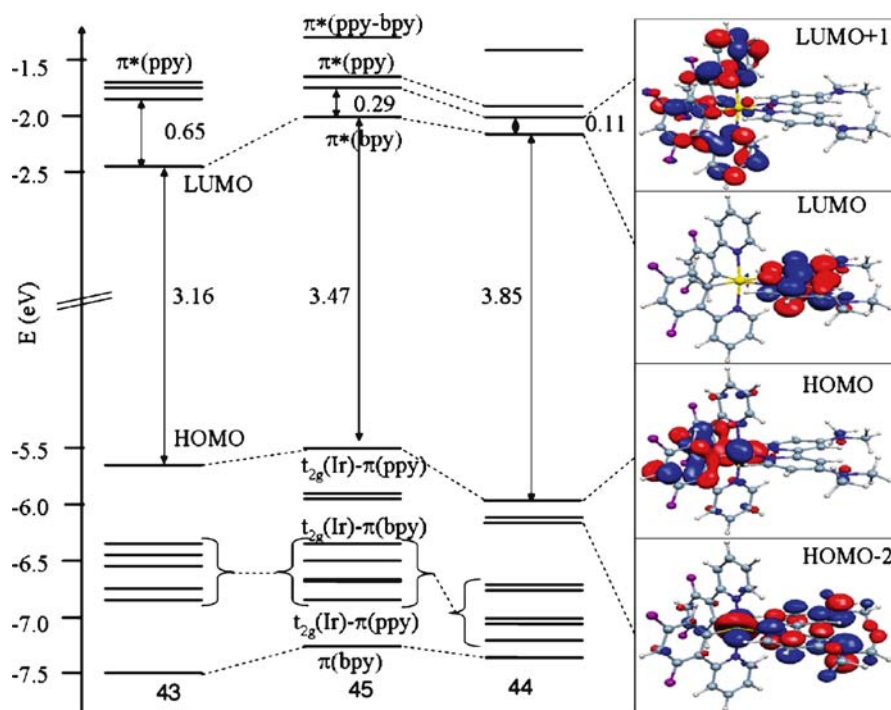

Fig. 27 Energy and character of the frontier molecular orbitals of **43**, **45**, and **44** complexes. Also shown are isodensity plots of selected molecular orbitals

2.5
Tuning of Phosphorescence Colors in Anionic Iridium Complexes

The tuning aspects of phosphorescence colors in anionic Ir complexes are illustrated using the following representative complexes: The $(C_4H_9)_4N[Ir(2-$ phenylpyridine$)_2(CN)_2]$ **(46)**, $(C_4H_9)_4N[Ir(2-phenyl)-4-dimethylaminopyr-$ idine$)_2(CN)_2]$ **(47)**, $(C_4H_9)_4N[Ir(2-(2,4-difluorophenyl)-pyridine)_2(CN)_2]$ **(48)**, $(C_4H_9)_4N[Ir(2-(2,4-difluorophenyl)-4-dimethylaminopyridine)_2(CN)_2]$ **(49)**, and $(C_4H_9)_4N[Ir(2-(3,5-difluorophenyl)-4-dimethylaminopyridine)_2$ $(CN)_2]$ **(50)** (Klein et al., unpublished data). All these complexes were con- veniently synthesized in low-boiling dichloromethane by reaction of the dichloro-bridged Ir(III) dimer with tetrabutylammonium cyanide. The crys- tal structure of complex **46** shows that the cyanide ligands coordinate through the carbon atom and adopt a *cis* configuration (Fig. 28).

Table 4 shows a comparison of the photophysical and electrochemical properties of complexes **46–50** that were measured in dichloromethane solu- tion at 298 K. When these complexes are excited within the $\pi-\pi^*$ and MLCT
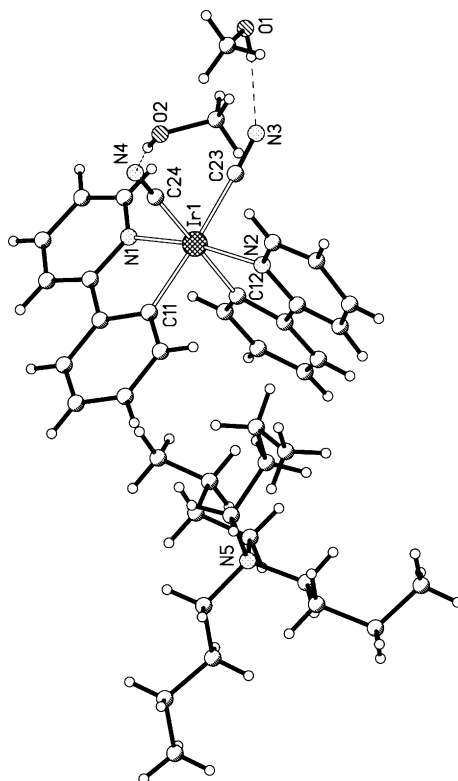

Fig. 28 Crystal structure of $(C_4H_9)_4N[Ir(2-phenylpyridine)_2(CN)_2]$ **46**

Table 4 Structures, absorption, emission, quantum yields, lifetime, and electrochemical data of complexes **46–50** measured at 298 K in dichloromethane solution

Complex	Absorption[a] λ_{max} (nm)	Emission[b] λ_{max} (nm)	Lifetime $E_{1/2ox}$ (μs)	Potential vs. Fc$^{+/0}$ $E_{1/2red}$ (V)	(V)
46	260 (41.7), 337 (0.85), 384 (0.58), 433sh (0.61) 463 (0.21)	470, 502	3.3	0.55	– 2.69
47	272 (3.79), 302sh (2.21), 332 (1.07), 354 (0.89), 380 (0.59)	465, 488	2.0	0.33	– 3.0
48	254 (6.04), 290 (2.79), 362 (0.78), 390 (0.38)	460, 485	3.3	0.96	– 2.6
49	266 (2.83), 290 (2.63), 302 (2.38), 338 (1.32), 360 (1.08)	451, 471	1.4	0.58	– 2.98
50	268 (5.25), 288 (4.20), 302sh (3.22), 356 (1.52), 378 (0.95)	468, 492	3.0	0.53	– 2.8

[a] Brackets contain values for molar extinction coefficient (ε) in $10^4 \, M^{-1} \, cm^{-1}$
[b] Emission spectra were obtained from degassed solutions by exciting into the lowest MLCT band

absorption bands, they show emission maxima in the blue and yellow regions of the visible spectra. The air-equilibrated dichloromethane solutions exhibit shorter luminescence lifetimes (70–90 ns) compared to the degassed solutions (1–3 μs). It is apparent from the photoluminescence data, which were obtained by exciting at 380 nm, that the complexes **46–50** show a color range from brilliant blue to yellow, unraveling the tuning aspect of the HOMO and the LUMO levels.

The LUMO levels of complex **47** are destabilized by incorporating dimethylamino group at the 4-position of pyridine. In complex **48** the HOMO levels are stabilized by insertion of fluoro substituents on the phenyl ring of the ppy ligand. However, in complex **49** both aspects (i.e., destabilization of the LUMO orbitals by incorporating a dimethylamino group at the 4-position of pyridine together with stabilization of HOMO orbitals by insertion of fluoro substituents on the phenyl of the ppy ligand) lead to an increase of the HOMO–LUMO gap accompanied by a blue shift of the emission spectra. Figure 29 shows a representative absorption and emission spectra of complex **49** measured in dichloromethane solution at 298 K. The complex displays bands in the UV and the visible region due to intraligand (π–π^*) and MLCT transitions, respectively [107]. When excited within the π–π^* and MLCT absorption bands at 298 K, complex **49** shows emission maxima at 450 and
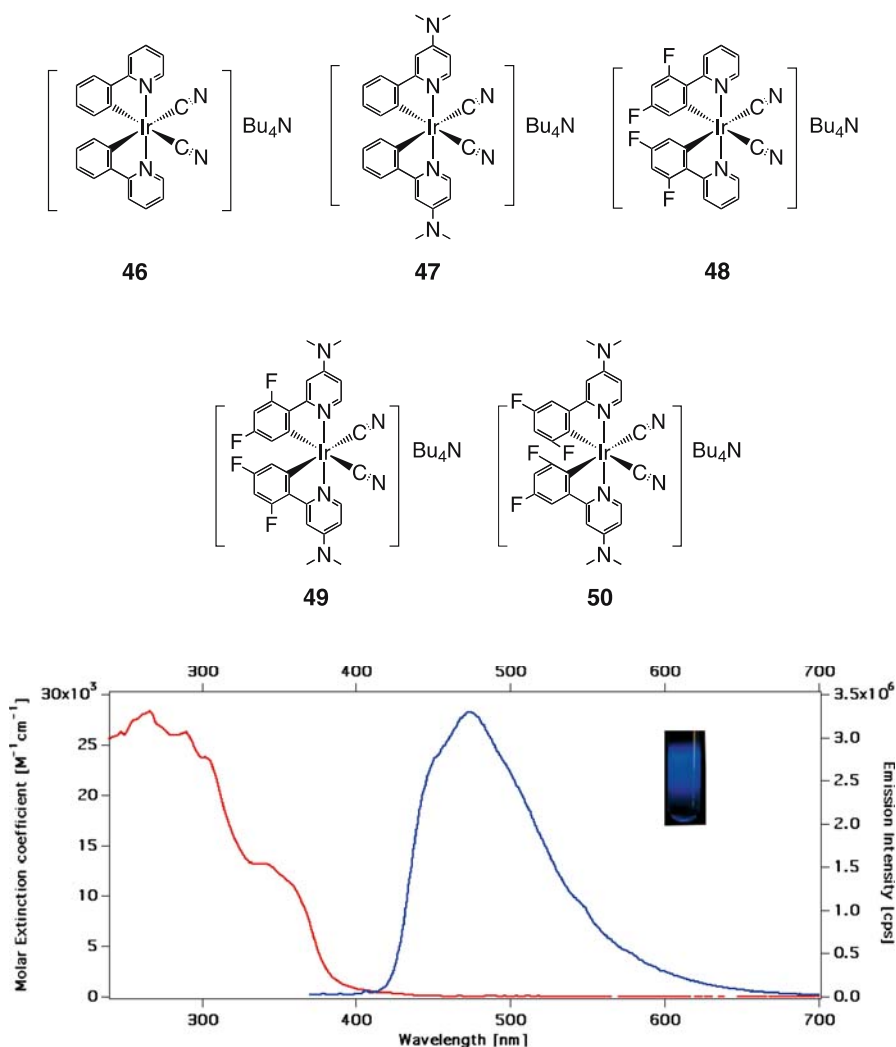
Fig. 29 Absorption (*red line*) and emission (*blue line*) spectra of complex **49** in dichloromethane solution at 298 K. The *insert* shows a photo of a solution of **49** exhibiting very strong blue emission upon excitation at 380 nm

473 nm due to the 2,4-difluorophenyl-4-dimethylaminopyridine ligand that increases the HOMO–LUMO gap resulting in a blue shift of the emission maxima compared to complexes **47** and **48**.

The difference between complexes **49** and **50** is only in the position of the fluoro substituent on the phenyl ring of the ppy ligand, which are at the 2,4-position in the former and the 3,5-position in the latter. The emission maxima of complex **50** is significantly red-shifted compared to complex **49**, demon-

strating the influence of substituent position on the photophysical properties. One possible explanation for this astonishing spectral shift of complex **50** compared to complex **49** is that the fluoro groups at the 3,5-position act as electron-releasing groups, destabilizing the metal HOMO orbitals and thereby decreasing the HOMO–LUMO gap. In complex **49**, the fluoro groups are at the 2,4-positions and act as electron-withdrawing groups, resulting in stabilization of HOMO orbitals and thereby increasing the HOMO–LUMO gap.

2.5.1
Phosphorescent Color Shift in Anionic Iridium Complexes by Tuning of HOMO Levels

Figure 30 shows schematically the concept of HOMO level tuning in Ir pseudohalogen complexes of the type TBA[Ir(ppy)$_2$(CN)$_2$] (**46**), TBA[Ir(ppy)$_2$
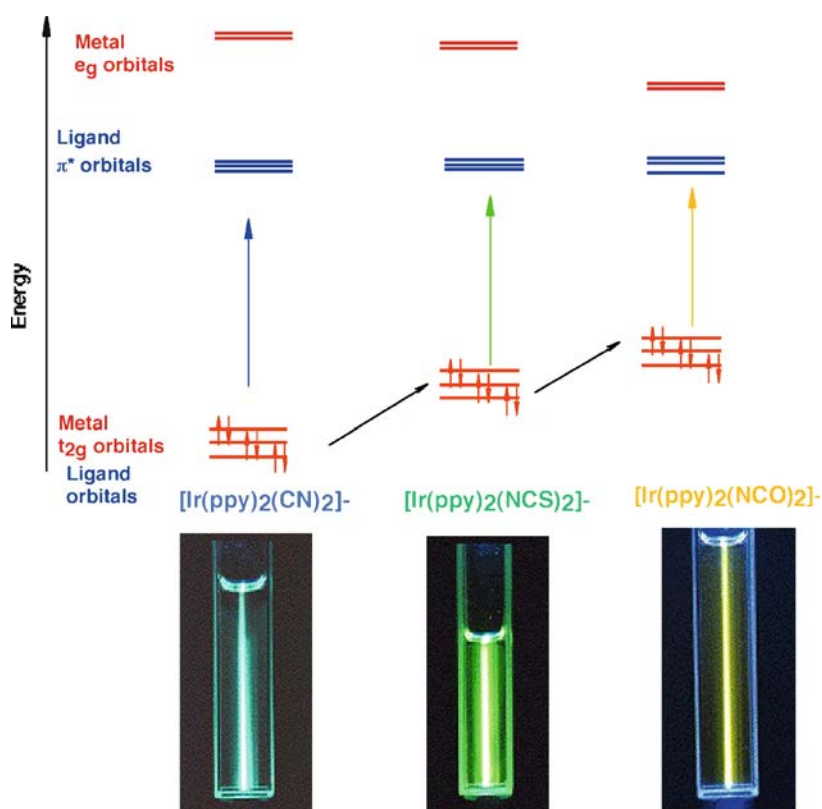

Fig. 30 Schematic drawing of HOMO and LUMO orbitals for complexes **46**, **51**, and **52** and their phosphorescence properties, which were obtained by exciting at 415.4 nm using a krypton ion laser

(NCS)$_2$] (**51**), and TBA[Ir(ppy)$_2$(NCO)$_2$] (**52**). These complexes were conveniently synthesized under inert atmosphere by reaction between the dichloro-bridged Ir dimer [Ir(ppy)$_2$(Cl)]$_2$ in dichloromethane solvent with an excess of a pseudohalogen ligand such as tetrabutylammonium cyanide, tetrabutylammonium thiocyanate, or tetrabutylammonium isocyanate, respectively, with over 70% yields [77].

The cyclic voltammograms of **46**, **51**, and **52** show a quasi-reversible oxidation potential at 0.91, 0.45, and 0.18 V vs. ferrocenium-ferrocene, respectively. Changes in the electron-donating or electron-withdrawing nature of the ancillary ligands can result in a variation of electronic properties at the metal center. It is interesting to compare these three complexes that contain cyanide, thiocyanate, and isocyanate ligands. The 0.73 V anodic shift in oxidation potential of **46** compared to complex **52** shows the extent of π back-bonding to the cyanide ligand from the Ir(III) center. The enormous enhancement in π back-bonding leads to significant blue shift of the emission maxima of complex **46** compared to complexes **51** and **52**.

The absorption spectra of these complexes display bands in the UV and the visible region due to intraligand (π–π^*) and MLCT transitions, respectively [107]. The MLCT band in **46** (463 nm) is significantly blue-shifted compared to **51** (478 nm), and **52** (494 nm), indicating the extent of π-acceptor strength of the CN$^-$ ligand compared to the NCS$^-$ and NCO$^-$ ligands. The spectral shifts are consistent with the electrochemical data of these complexes. Hay has analyzed the spectral properties of Ir(III)ppy complexes using DFT, in which the low-lying transitions are categorized as MLCT transitions and the high-energy bands at above 280 nm are assigned to the intraligand

Table 5 Emission, lifetime, and quantum yield data of complexes **46**, **51**, and **52** measured at 298 K in dichloromethane

Complex	Absorption[a] λ_{max} (nm)	Emission[b] λ_{max} (nm)	Emission ϕ_f	Lifetime τ (μs)	Potential vs. Fc$^{+/0}$ $E_{1/2ox}$ (V)
46	260 (41.7), 337 (0.85), 384 (0.58), 463 (0.21)	470, 502	0.94	3.1	0.91
51	266 (38.9), 335 (6.7), 355 (5.3), 400 (3.4), 476 (0.65),	506, 520	0.97	1.4	0.45
52	276 (35.1), 347 (6.62), 384 (4.22), 408 (3.41), 464 (2.36), 497 (1.26)	538, 560	0.99	0.8	0.18

[a] Brackets contain values for molar extinction coefficient (ε) in 10^4 M^{-1} cm^{-1}
[b] Emission spectra were obtained from degassed solutions by exciting into the lowest MLCT band

$\pi-\pi^*$ transitions of ppy [95]. Argon-degassed solutions of complexes **46**, **51** and **52**, when excited within the $\pi-\pi^*$ and MLCT absorption band at 298 K, show emission maxima at 470, 506 and 538 nm, respectively with longer lifetimes (0.8–3.4 μs) (Table 5).

2.6
Controlling Quantum Yields in Iridium Complexes

Orthometalated Ir complexes are known to have highest triplet emission quantum yields due to several factors [109, 110]:

- Ir has a large d-orbital splitting compared to other metals in the group
- Strong ligand field strength of the ppy anionic ligand increases the d-orbital splitting, leading to an enlarged gap between the e_g orbitals of Ir and the LUMO of the ligand
- Close-lying $\pi-\pi^*$ and MLCT transitions, together with the heavy atom effect, enhance the spin-orbit coupling

However, the mixed ligand cationic Ir complexes show appreciably lower quantum yields compared to the tris-orthometalated Ir complexes because of the lower LUMO orbitals of the $2,2'$-bipyridine ligand [78, 85, 96]. One strategy to increase the quantum yields of Ir complexes is to introduce F and/or CF_3 substituents. This results in a stabilization of both the HOMO and the LUMO. Since the HOMO stabilization is larger than that of the LUMO, this leads to an increase in the gap between HOMO–LUMO [111]. Another strategy, however, is to decrease the gap between the lowest π^* orbitals of the ppy ligand and the $2,2'$-bipyridine ligand by introducing donor substituents such as dimethylamino groups at the $4,4'$-positions of $2,2'$-bipyridine that are known to have a strong destabilization effect on the LUMO (see complexes **44** and **45**). In such type of complexes, the $\pi-\pi^*$ and MLCT states associated with the ppy and $4,4'$-dimethylamino-$2,2'$-bipyridine ligands are expected to be located closely together, which enhances the excited state decay through radiative pathways.

The quantum yields of complexes **44** and **45** were measured using recrystallized quinine sulfate in 1 N H_2SO_4 and the widely referred complex $Ru(bpy)_3(PF_6)_2$ as quantum yield standards. The data obtained using both standards are in excellent agreement and indeed show yields that are remarkably high, i.e., 80%.

The quantum yields of Ir complexes can also be modulated by introducing ligands having strong ligand field stabilization energy, such as NCS^- and CN^-. In these complexes, the gap between the metal e_g and the ligand LUMO orbitals increases, resulting in a decay of the excited charge transfer states through radiative pathways [77].

2.7
Application of Iridium Complexes
in Organic Light Emitting Devices

Doping of the emitting layer of OLEDs with well-selected dye molecules is an established way to improve OLED performance. To clarify, in the context of this article, from what we understand doping is not the introduction of additional charges as in the classical semiconductor sense but rather the introduction of dye molecules with appropriate energy levels for color tuning. Besides this aspect, doping also leads to a change of the transport characteristics and to a considerable increase of the lifetime and of the quantum efficiency.

For a long time people thought that the luminescent dyes used since the work of Tang et al. are theoretically limited to an internal conversion efficiency of 25% [112]. This factor arrives from quantum mechanics, where 75% of the charge wave functions are of the non-emissive triplet case and only 25% of the singlet case, allowing radiative recombination. Taken into account that only one-fifth of the created photons can leave the device, the external quantum efficiency was limited to 5% [113]. But, in contrast to this, the family of the so-called phosphorescent dyes (triplet emitters) permits the opening of an additional radiative recombination channel and harvesting of up to nearly 100% of the excited states to photon creation. Responsible for this is the presence of heavy metal atoms such as Pt or Ir [114], leading to a strong spin-orbit coupling. The common way of device realization is to a mix small concentration of a highly phosphorescent guest into a host material with suitable charge transport abilities. Taking into account an unchanged out-coupling factor of one-fifth, the theoretical external quantum efficiency for the triplet dyes jumps up to 20%. Electrophosphorescence was shown for the first time by Hoshino et al. by mixing benzophenone into a poly(methylmethacrylate) host [115], but the quantum efficiency was still low. Meanwhile, quantum efficiencies up to the theoretical limits are reported in the literature [114].

Typical dye doping concentrations of singlet and triplet emitters are very different. For singlet emitters the efficient doping ratio is often limited to the range 0.5–2%, as for example 1.3% for Rubrene in tris(8-hydroxyquinolato)aluminum (Alq$_3$) [116] or 0.7% for DEQ in Alq$_3$ [117]. For triplet emitter dyes, doping ratios up to 10% or far above are possible without remarkable loss in quantum efficiency [118]. Increased doping concentrations of triplet emitters are desirable to prevent or reduce saturation effects at increased current densities due to the long lifetimes of the excited states [119]. But, high doping concentrations are accompanied by side effects. To have the dye molecules with appropriate behavior inside the matrix is one point; the other point is that the dye molecule should also be able to localize the exciton. In principle three techniques are discussed to get the exciton on the dye dopant: (i) endothermic energy transfer [120], (ii) exothermic energy trans-

fer [121], and (iii) charge trapping as it applies for heavily doped systems and for blue phosphorescent devices [119].

Another aspect is that large energy gap matrixes are desired to suppress both the electron and energy transfer pathways from the emissive dopant back to the host material [122]. Pai et al. observed the transition from hole hopping between host molecules to trap-controlled tunneling transport as a function of doping concentration [123]. At concentrations of the additive below 2 wt. %, the transport is dominated by the slow release of charges from the dye sites acting as charge traps. For concentrations above 2 wt. % hopping occurs via trap and host sites. As the trap concentration is further increased, the transport by tunneling via the additive sites becomes predominant.

The long lifetime of the triplet excitons enables them theoretically to diffuse significant distances. To reduce this, typical diode architectures, including phosphorescent emitters, require at least one more auxiliary layer (such as a hole blocking layer) than a fluorescent emitter containing diode. Further, the energy levels of the host should be significantly higher to localize the excitons on the dopant [119]. This approach will be discussed in the following section in more detail.

2.7.1
Standard OLED Device Architecture

A typical multilayer device architecture containing triplet emitters is described in Fig. 31, and the resulting energy level scheme is shown in Fig. 32. ITO (indium tin oxide)-coated glass substrate is used as anode and on top of it a 10 nm thick CuPc (copper phthalocyanine) hole injection layer is
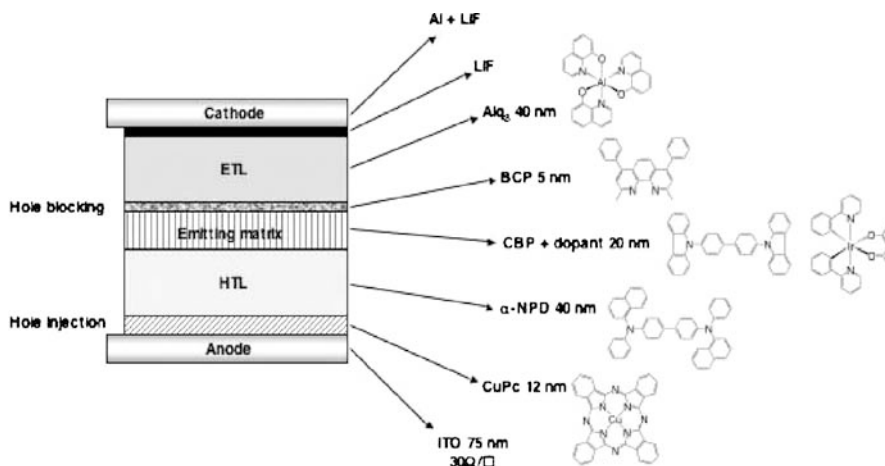

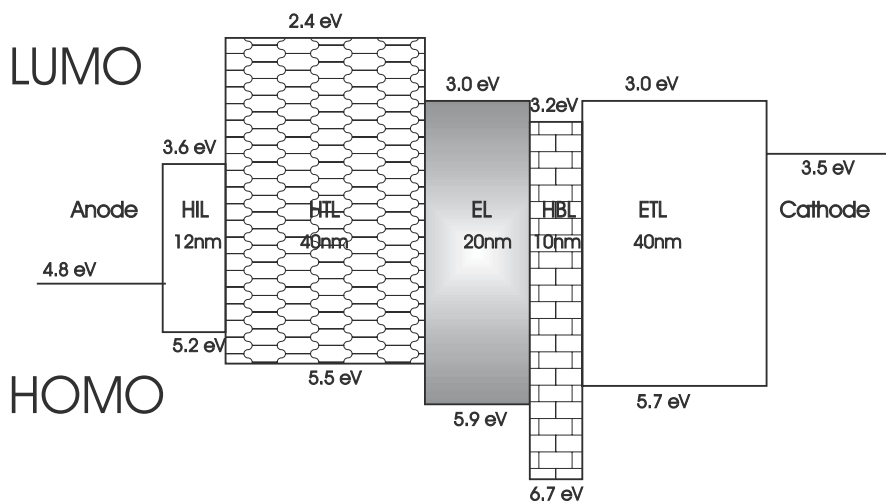**Fig. 31** Cross-section of the OLED device

LUMO

2.4 eV

3.0 eV   3.0 eV

3.2eV

3.6 eV

3.5 eV

Anode   HIL   HTL   EL   HBL   ETL   Cathode

        12nm   40nm   20nm   10nm   40nm

4.8 eV

5.2 eV

5.5 eV

HOMO

5.9 eV

5.7 eV

6.7 eV

Fig. 32 Typical electrophosphorescent multilayer device architecture composed of a hole injection layer (*HIL*), a hole transport layer (*HTL*), a emission layer (*EL*), a hole blocking layer (*HBL*), an electron blocking layer (*EBL*), and finally an electron transporting layer (*ETL*). Shown are the HOMO and LUMO energy levels of the corresponding molecules [77]. The vacuum level is assumed to be constant

deposited. Next, a 40 nm thick hole transport layer of α-NPD (*N,N′*-diphenyl-*N,N′*-bis(1-naphthyl)-1,1′-biphenyl-4,4′-diamine) is evaporated, followed by a 20 nm layer of the wide energy-gap matrix of CBP (4,4′-bis(carbazol-9-yl)-biphenyl) co-evaporated with a constant rate of a phosphorescent emitter molecule. For hole blocking and resulting charge confinement in the emitting matrix layer, a 5 nm layer of BCP (2,9-dimethyl-4,7-diphenyl-phenanthroline) can be useful for quantum efficiency improvement. Finally, a 30–40 nm thick Alq$_3$ electron transport layer is deposited to improve the out-coupling efficiency [124] and to reduce exciton quenching by the metallic cathodes [114]. For performance improvement, the organics should be purified and thermally evaporated at a rate of $1.0\,\text{Å}\,\text{s}^{-1}$ at a base pressure lower than 10^{-6} mbar. A well-working cathode for such architecture consists of a 0.8 nm LiF layer deposited right after the electron transporting layer (ETL) in combination with a 100 nm thick Al layer. To decrease contamination effects and impurity layers the whole fabrication should be done without breaking the vacuum. The active area of engineering segments is in the range 4–10 mm^2.

    The presented standard device architecture doped with different ratios of the phosphorescent emitter molecule [acetylacetonato-(bis(2-phenylpyridine) Ir(III))], labeled as complex **53**, is used as a model case. Figure 33 shows the different current–voltage characteristics for complex **53** doped in CBP-host for doping concentrations ranging from zero to 12 mol %. The voltage region below ≈ 2.5–3 V is characterized by a single carrier-type transport, and
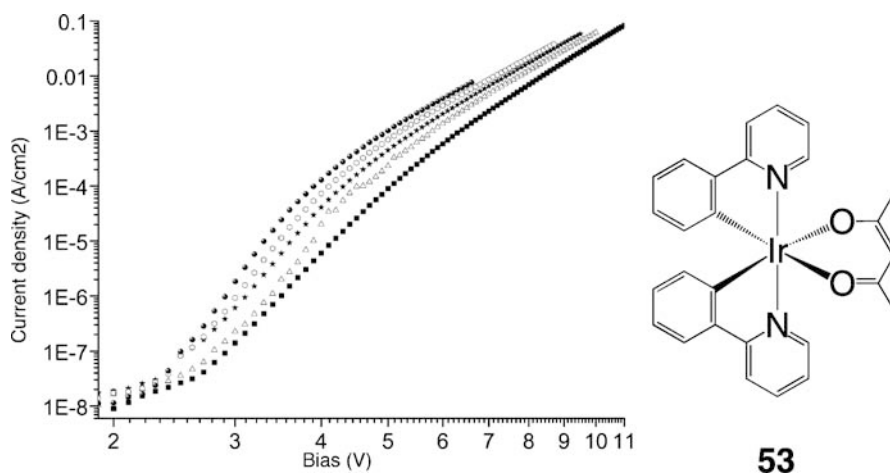
Fig. 33 Current versus voltage characteristics for different doping concentrations of phosphorescent dye **53** in a CBP matrix

the exact value depends on the doping concentration. Above this threshold voltage, a steep increase in the diode current corresponding to two-carrier injection is observed, which leads to light generation. The lower current threshold field ($U_{th\,1}$), here defined as the voltage for a current of $1\,\mu A\,cm^{-2}$, decreases monotonously from 3.5 V for the undoped case to 2.9 V for maximum doping of 12 mol %. This indicates that the dye molecules seem to improve carrier injection into the matrix layer. The energy barrier for holes at the α-NPD/CBP interface is 0.43 eV (HOMO–HOMO barrier). However, the energy barrier from α-NPD to complex **53** is negligible, i.e., less than 0.1 eV [HOMOs of α-NPD = 5.53 eV, CBP = 5.96 eV and of complex **53** = 5.6 eV] [77]. For higher doping concentrations this injection and transport mechanism is even improved. The energy barriers for the electrons are less important for all organic/organic interfaces (≤ 0.2 eV).

Furthermore, by direct charge injection from the adjacent hole and electron transport layers onto the phosphor molecule doped into the wide energy-gap matrix, exciton formation occurs directly on the dopant. In other words, in this image it is not the efficiency of the energy transfer from the host to the dye dopant, it is rather injection of the holes onto the dopant where they have "only" to wait for the electron. As already pointed out, it is a function of dye concentration if the charge jumps from dye to dye or if it is energetically favorable for the charge to detrap by jumping from the dye to the host [125].

Figure 34 shows the variation of the quantum efficiency as a function of the doping concentration. We see a slight variation for concentrations between 3 and 12% with its maximum at 9% and 13.2% of external quantum efficiency. For comparison, in the undoped case the quantum efficiency is only 0.94%.
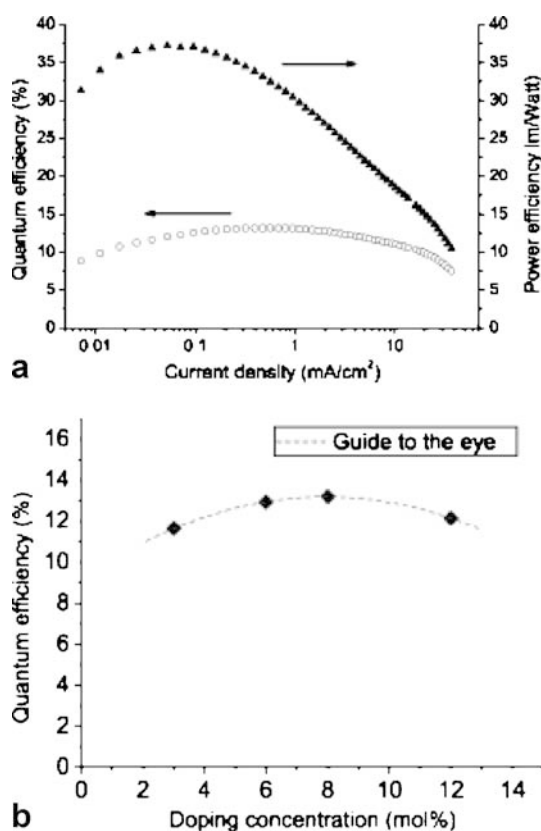
Fig. 34 a External quantum and power efficiencies versus current. **b** External quantum efficiency as a function of the doping concentration

This corresponds to an improvement of around one and a half orders of magnitude. Still more impressive is the improvement in the power efficiency, which increases from $0.65 \, \mathrm{lm \, W^{-1}}$ for the undoped case (not presented) up to $37 \, \mathrm{lm \, W^{-1}}$ for the 9% doped case, which represents an improvement factor of 56. These values are close to the values cited in the recent literature [76]. However, they are lower than the best values achieved with triplet emitters in a TAZ-host [126]. A reason could be that the very low TAZ HOMO level of $-6.6 \, \mathrm{eV}$ favors direct injection and transport at the dopant level and therefore the exciton escaping rate from the dopant to the host becomes negligible. This impressive value of quantum efficiency is based on a well-balanced charge ratio inside the emission layer, without any leaking current to the anode nor to the cathode side. Other experiments by Berner et al. [127] have shown how to get nearly equalized charge balance by using ITO/CuPc on the anode side and LiF/Al on the cathode side, taking into account the hole-blocking capabilities of BCP and the electron-blocking capabilities of α-NPD [128–131].
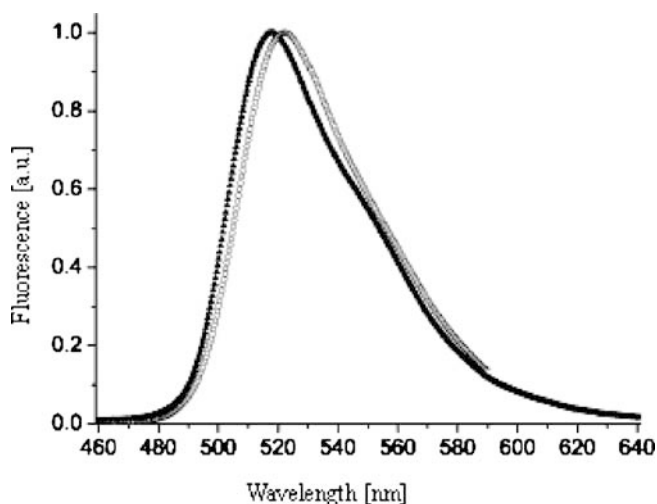
Fig. 35 Electrophosphorescence of complex **53** in a CBP matrix for the 3% (*black line*) and 12% (*gray line*) doped cases are shown. Additionally, the luminance versus voltage is presented for the 9% doped case

For the 6 mol % doped device the number of dopant molecules inside the doped volume can be calculated with the hypothesis of homogeneous distribution of the molecules. With 12 μs of the averaged lifetime of the excited state of complex **53** and the additional assumption of homogeneous distribution of excited molecules, the upper level of the effective distance between excited molecules as a function of the current density can be estimated. Thereby, the charge density distribution was admitted to half of the doped zone, which is a reasonable assumption as demonstrated by model calculations [127]. This effective distance is directly related to the current-dependent quantum efficiency $\eta_{(I)}$ of the device.

Figure 35 shows the electrophosphorescence spectra of complex **53** for 3% and 12% doped in CBP. A slight red shift for increasing doping concentration is seen, but the emission spectra were independent of current densities up to 150 mA cm^{-2}. The same emission peak is found from a solution phosphorescence spectra of complex **53**. The emission peaks of α-NPD and the host, which are located in the blue at around 440–450 nm and around 480 nm, or intermediate exciplexes are not present. Another characteristic of phosphorescent dyes is the considerable reduction of the linewidth of the emission spectra compared to standard luminescence materials like Alq$_3$. In the case of complex **53**, the line width is only 52 nm (compared to an undoped Alq$_3$ emission where the line width is 83 nm), which leads to the saturated color that is necessary for high-performance color displays, assuming that the emission maximum is well located around one of the primary colors green, blue, or red.

2.8
Light-Emitting Electrochemical Cell Device Architecture

Another type of organic light emitting device is the light-emitting elec-
trochemical cell (LEC), which makes use of ionic charges to facilitate
electronic charge injection from the electrodes into the organic molecu-
lar semiconductor, eliminating the need for extra layers [78–82, 132]. This
is a promising alternative to OLED, particularly for large-area lighting
applications [82, 133–135]. In these cells a thicker organic active layer can
be used, while keeping the operating voltage low, and a low-workfunction
metal electrode is not needed. Recently, cationic Ir complexes **43** and **45** were
incorporated in LECs leading to yellow [136] and blue-green [49, 111] electro-
luminescence.

To investigate the electroluminescence properties of the cationic complex **45**
[Ir(2-phenylpyridine)$_2$(4,4′-dimethylamino-2,2′-bipyridine)]PF$_6$, LECs were
fabricated in a nitrogen atmosphere glovebox [82]. They consisted of a 100 nm
spin-coated layer of pristine **45** sandwiched between an ITO and an evaporated
Ag electrode [106].

It is well known that solid-state LECs exhibit a significant response time
since electroluminescence can only occur after the ionic double-layers have
been built up at the electrode interfaces [79, 82]. Since in this case only the
PF$_6^-$ anion is mobile, the double-layers are formed by accumulation and de-
pletion of PF$_6^-$ at the anode and cathode, respectively. The LEC device with
45 started to emit blue-green light at a bias of 5 V after several minutes. The
electroluminescence spectrum, as shown in Fig. 36 (trace a), is very similar
to the photoluminescence spectrum recorded for a spin-coated film on glass
and of a solution of the complex. For comparison, the electroluminescence
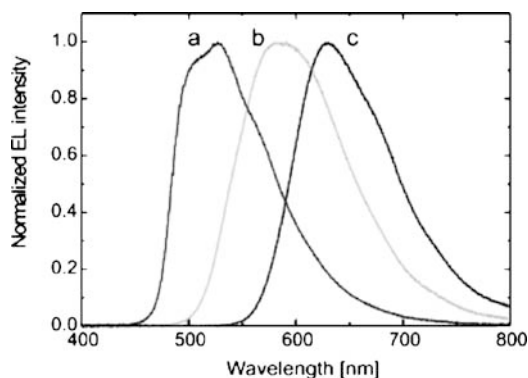

Fig. 36 Electroluminescence spectra of ITO/EL layer/Ag devices, where the EL layer con-
sists of [Ir(ppy)$_2$(dma-bpy)]PF$_6$ (*a*), [Ir(ppy)$_2$(bpy)]PF$_6$ + PMMA (*b*), and [Ru(bpy)$_3$]
(PF$_6$)$_2$ + PMMA (*c*)

spectra recorded for similar devices with $[Ir(ppy)_2(bpy)]PF_6$ (trace b, yellow emission) and $[Ru(bpy)_3](PF_6)_2$ (trace c, orange/red emission) as active material are also shown [82]. The fact that blue-green emission is obtained with an Ag cathode at a voltage as low as 2.5 V indicates the power of the LEC behavior.

References

1. Hagfeldt A, Grätzel M (2000) Acc Chem Res 33:269
2. West W (1974) Proc Vogel Cent Symp Photogr Sci Eng 18:35
3. Moser J (1887) Notiz über die Verstärkung photoelectrischer Ströme durch optische Sensibilisierung. Monatsh Chemie 8:373
4. Namba S, Hishiki Y (1965) J Phys Chem 69:774
5. Gerischer H, Tributsch H (1968) Phys Chem 72:437
6. Dare-Edwards MP, Goodenough JB, Hamnett A, Seddon KR, Wright RD (1981) Faraday Discuss Chem Soc 70:285
7. Tsubomura H, Matsumura M, Nomura Y, Amamiya T (1976) Nature 261:402
8. Dunghong D, Serpone N, Graetzel M (1984) Helv Chim Acta 67:1012
9. Desilvestro J, Graetzel M, Kavan L, Moser J, Augustynski J (1985) J Am Chem Soc 107:2988
10. O'Regan B, Grätzel M (1991) Nature 353:737
11. Nazeeruddin MK, Wang Q, Cevey L, Aranyos V, Liska P, Figgemeier E, Klein C, Hirata N, Koops S, Haque SA, Durrant JR, Hagfeldt A, Lever ABP, Grätzel M (2006) Inorg Chem 45:787
12. Barbé CJ, Arendse F, Comte P, Jirousek M, Lenzmann F, Shklover V, Grätzel M (1997) J Am Ceram Soc 80:3157
13. Rothenberger G, Comte P, Graetzel M (1999) Solar Energ Mater Solar Cells 58:321
14. Burnside SD, Shklover V, Barbe CJ, Comte P, Arendse F, Brooks K, Grätzel M (1998) Chem Mater 10:2419
15. Hagfeldt A, Grätzel M (1995) Chem Rev 95:49
16. Cahen D, Hodes G, Grätzel M, Guilemoles JF, Riess I (2000) J Phys Chem B 104:2053
17. Ferber J, Luther J (2001) J Phys Chem B 105:4895
18. van de Lagemaat J, Park N-G, Frank AJ (2000) J Phys Chem B 104:2044
19. Nazeeruddin MK, Kay A, Rodicio I, Humphry-Baker R, Muller E, Liska P, Vlachopoulos N, Grätzel M (1993) J Am Chem Soc 115:6382
20. Grätzel M (2001) Nature 414:338
21. Nazeeruddin MK, Grätzel M (2003) In: Ramamurthy V, Schanze KS (eds) Molecular and supramolecular photochemistry, vol 10. Dekker, New York, p 301
22. Nazeeruddin MK (2004) In: Nazeeruddin MK (ed) Special issue: Michael Graetzel Festschrift, A tribute for his 60th birthday: Dye sensitized solar cells. Coord Chem Rev 248:1161
23. Grätzel M (2000) In: Nalwa HS (ed) Handbook of nanostructured materials and nanotechnology, vol 3. Academic, New York, p 527

24. Haught AF (1984) J Solar Energ Eng 106:3
25. De Vos A (1992) Endoreversible thermodynamics of solar energy conversion. Oxford Science, Oxford, chap 6
26. Nazeeruddin MK, Zakeeruddin SM, Humphry-Baker R, Jirousek M, Liska P, Vlachopoulos N, Shklover V, Fischer CH, Grätzel M (1999) Inorg Chem 38:6298
27. Anderson S, Constable EC, Dare-Edwards MP, Goodenough JB, Hamnett A, Seddon KR, Wright RD (1979) Nature 280:571
28. Anderson PA, Strouse GF, Treadway JA, Keene FR, Meyer TJ (1994) Inorg Chem 33:3863
29. Hara S, Sugihara H, Tachibana Y, Islam A, Yanagida M, Sayama K, Arakawa H (2001) Langmuir 17:5992
30. Nazeeruddin MK, Graetzel M (2002) In: Licht S (ed) Semiconductor electrodes and photoelectrochemistry. Encyclopedia of electrochemistry, vol 6. Wiley, Weinheim (pp 407–431)
31. Balzani V, Juris A, Venturi M, Campagna S, Serroni S (1996) Chem Rev 96:759
32. Kalyanasundaram K, Nazeeruddin MK (1992) Chem Phys Lett 193:292
33. Nazeeruddin MK, Muller E, Humphry-Baker R, Vlachopoulos N, Grätzel M (1997) J Chem Soc, Dalton Trans, p 4571
34. Nazeeruddin MK, Grätzel M, Kalyanasundaram K, Girling RB, Hester RE (1993) J Chem Soc, Dalton Trans, p 323
35. Zakeeruddin SM, Nazeeruddin MK, Pechy P, Rotzinger FP, Humphry-Baker R, Kalyanasundaram K, Grätzel M (1997) Inorg Chem 36:5937
36. Nazeeruddin MK, Pe'chy P, Renouard T, Zakeeruddin SM, Humphry-Baker R, Comte P, Liska P, Le C, Costa E, Shklover V, Spiccia L, Deacon GB, Bignozzi CA, Grätzel M (2001) J Am Chem Soc 123:1613
37. Nazeeruddin MK, Zakeeruddin SM, Humphry-Baker R, Gorelsky SI, Lever ABP, Graetzel M (2000) Coord Chem Rev 208:213
38. Masood MA, Sullivan BP, Hodges DJ (1994) Inorg Chem 33:5360
39. Durham B, Wilson SR, Hodges DJ, Meyer TJ (1980) J Am Chem Soc 102:600
40. Tennakone K, Kumara GRRA, Kottegoda IRM, Perera VPS (1999) Chem Commun, p 15
41. Chandrasekharan N, Kamat PV (2000) J Phys Chem B 104:10851
42. Gregg BA, Pichot F, Ferrere S, Fields CL (2001) J Phys Chem B 105:1422
43. Schmidt-Mende L, Kroeze J, Durrant JR, Nazeeruddin MK, Grätzel M (2005) NANO-LETTERS 5:1315
44. Nazeeruddin MK, Klein C, Liska P, Grätzel M (2005) Coord Chem Rev 248:1317
45. Nazeeruddin MK, De Angelis F, Fantacci S, Selloni A, Viscardi G, Liska P, Ito S, Bessho T, Grätzel M (2005) J Am Chem Soc 127:16835
46. Nazeeruddin MK, Wang Q, Cevey L, Aranyos V, Liska P, Figgemeier E, Klein C, Hirata N, Koops S, Haque SA, Durrant JR, Hagfeldt A, Lever ABP, Grätzel M (2006) Inorg Chem 45:787
47. Wang P, Klein C, Humphry-Baker R, Zakeeruddin SM, Grätzel M (2005) Appl Phys Lett 86:123508
48. Renouard T, Fallahpour R-A, Nazeeruddin MK, Humphry-Baker R, Gorelsky SI, Lever ABP, Grätzel M (2002) Inorg Chem 41:367
49. Barolo C, Nazeeruddin MK, Fantacci S, Di Censo D, Ito S, Comte P, Liska P, Viscardi G, Quagliotto P, De Angelis F, Grätzel M (2006) Inorg Chem 45:4642
50. Lever ABP (1990) Inorg Chem 29:1271
51. Wolfbauer G, Bond AM, Deacon GB, MacFarlane DR, Spiccia L (2000) J Am Chem Soc 122:130

52. Bignozzi CA, Aragazzi R, Kleverlaan CJ (2000) Chem Soc Rev 29:87
53. Trammell SA, Moss JA, Yang JC, Nakhle BM, Slate CA, Odobel F, Sykora M, Erickson BW, Meyer TJ (1999) Inorg Chem 38:3665
54. Tennakone K, Kumara GRRA, Wijayantha KGU (1996) Semicond Sci Technol 11:1737
55. Yan SG, Hupp JT (1996) J Phys Chem 100:6867
56. Yanagi H, Chen S, Lee PA, Nebesny KW, Armstrong NR, Fujishima A (1996) J Phys Chem 100:5447
57. Yanagi H, Fujishima A, Chen S, Lee PE, Nebesny KW, Amstrong NR (1996) J Phys Chem 100:5447
58. Will G, Boschloo G, Nagaraja Rao S, Fitzmaurice D (1999) J Phys Chem B 103:8067
59. Lemon B, Hupp JT (1999) J Phys Chem B 103:3797
60. Jing B, Zhang H, Zhang M, Lu Z, Shen T (1998) J Mater Chem 8:2055
61. Rice CR, Ward MD, Nazeeruddin MK, Grätzel M (2000) New J Chem 24:651
62. Murakoshi K, Kano G, Wada Y, Yanagida S, Miyazaki H, Matsumoto M, Murasawa S (1995) J Electroanal Chem 396:27
63. Finnie KS, Bartlett JR, Woolfrey JL (1998) Langmuir 14:2744
64. Fillinger A, Parkinson BA (1999) J Electrochem Soc 146:4559
65. Shklover V, Ovehinnikov YE, Braginsky LS, Zakeeruddin SM, Grätzel M (1998) Chem Mater 10:2533
66. Nazeeruddin MK, Humphry-Baker R, Liska P, Grätzel M (2003) J Phys Chem B 107:8981
67. Tachibana Y, Haque SA, Mercer IP, Moser JE, Klug DR, Durrant JR (2001) J Phys Chem B 105:7424
68. Chiba Y, Islam A, Watanabe Y, Komiya R, Koide N, Han L (2006) Japan J Appl Phys 2: Lett Expr Lett 45:24
69. Bach U, Lupo D, Compte P, Moser JE, Weissörtel F, Salbeck J, Spreitzer H, Grätzel M (1998) Nature 395:583
70. Ito S, Zakeeruddin SM, Humphry-Baker R, Liska P, Charvet R, Comte P, Nazeeruddin MK, Pechy P, Takata M, Miura H, Uchida S, Grätzel M (2006) Adv Mater 18:1202
71. Grätzel M (2006) Comptes Rendus Chimie 9:578
72. Hinsch A (2000) In: Scheel HJ (ed) Proc 16th Eur PV Solar Energ Conf, Glasgow, Vol. 32. James & James, London
73. Wang P, Zakeeruddin SM, Moser J, Nazeeruddin MK, Sekiguchi T, Graetzel M (2003) Nat Mater 2:402
74. Adachi C, Baldo MA, Thompson ME, Forrest SR (2001) J Appl Phys 90:5048
75. Baldo MA, Lamansky S, Burrows PE, Thompson ME, Forrest SR (1999) Appl Phys Lett 75:4
76. Ikai M, Tokito S, Sakamoto Y, Suzuki T, Taga Y (2001) Appl Phys Lett 79:156
77. Nazeeruddin MK, Humphry-Baker R (2003) J Am Chem Soc 125:8790
78. Slinker JD, Gorodetsky AA, Lowry MS, Wang J, Parker S, Rohl R, Bernhard S, Malliaras GG (2004) J Am Chem Soc 126:2763
79. Slinker J, Bernards D, Houston PL, Abruna HD, Bernhard S, Malliaras GG (2003) Chem Commun, p 2392
80. Rudmann H, Shimida S, Rubner MF (2002) J Am Chem Soc 124:4918
81. Bernhard S, Barron JA, Houston PL, Abruna HD, Ruglovksy JL, Gao X, Malliaras GG (2002) J Am Chem Soc 124:13624
82. Wegh RT, Meijer EJ, Plummer EA, De Cola L, Brunner K, van Dijken A, Hofstraat JW (2004) Proc SPIE 5519:48
83. Handy ES, Pal AJ, Rubner MF (1999) J Am Chem Soc 121:3525

84. Gao FG, Bard AJ (2000) J Am Chem Soc 122:7426
85. Yang C-H, Li S-W, Chi Y, Cheng Y-M, Yeh Y-S, Chou P-T, Lee G-H (2005) Inorg Chem 44:7770
86. Coppo P, Plummer EA, De Cola L (2004) Chem Commun, p 1774
87. Sajoto T, Djurovich PI, Tamayo A, Yousufuddin M, Bau R, Thompson ME, Holmes RH, Forrest SR (2005) Inorg Chem 44:7992
88. Lowry MS, Hudson WR, Pascal RAJ, Bernhard S (2004) J Am Chem Soc 126:14129
89. You Y, Park SY (2005) J Am Chem Soc 127:12438
90. Tmayo AB, Garon S, Sajoto T, Djurovich PI, Tsyba IM, Bau R, Thompson ME (2005) Inorg Chem 44:8723
91. Strickler SJ, Berg RA (1962) J Chem Phys 37:814
92. Kober EM, Caspar JV, Lumpkin RS, Meyer TJ (1986) J Phys Chem 90:3722
93. Juris A, Balzani V, Barigelletti F, Campagna S, Belser P, von Zelewsky A (1988) Coord Chem Rev 84:85
94. Nonoyama M (1975) Bull Chem Soc Jpn 47:767
95. Hay PJ (2002) J Phys Chem B 106:1634
96. King KA, Watts RJ (1987) J Am Chem Soc 109:1589
97. Dedeian K, Djurovich PI, Garces FO, Carlson C, Watts RJ (1991) Inorg Chem 30:1685
98. Sprouse S, King KA, Spellane PJ, Watts RJ (1984) J Am Chem Soc 6647
99. Yang CH, Li SW, Chi Y, Cheng YM, Yeh YS, Chou PT, Lee GH, Wang CH, Shu CF (2005) Inorg Chem 44:7770
100. Tsuboyama A, Iwawaki H, Furugori M, Mukaide T, Kamatani J, Igawa S, Moriyama T, Miura S, Takiguchi T, Okada S, Hoshino M, Ueno K (2003) J Am Chem Soc 125:12971
101. You Y, Park SY (2005) J Am Chem Soc 127:12438
102. Yeh S-J, Wu M-F, Chen C-T, Song Y-H, Chi Y, Ho M-H, Hsu S-F, Chen C-H (2005) Adv Mater 17:285
103. Hwang FM, Chen HY, Chen PS, Liu CS, Chi Y, Shu CF, Wu FL, Chou PT, Peng SM, Lee GH (2005) Inorg Chem 44:1344
104. Laskar IR, Hsu SF, Chen TM (2005) Polyhedron 24:189
105. Fang K-H, Wu L-L, Huang Y-T, Yang C-H, Sun IW (2006) Inorg Chem Acta 359:441
106. Nazeeruddin MK, Wegh RT, Zhou Z, Klein C, Wang Q, Fantacci S, De Angelis F, Graetzel M (2006) Inorg Chem 45:9245
107. Schmid B, Garces FO, Watts RJ (1994) Inorg Chem 33:9
108. Ichimura K, Kobayashi T, King KA, Watts RJ (1987) J Phys Chem 91:6104
109. Ohsawa Y, Sprouse S, King KA, DeArmond MK, Hanck KW, Watts RJ (1987) J Phys Chem 91:1047
110. Garces FO, King KA, Watts RJ (1988) Inorg Chem 27:3464
111. Lowry MS, Goldsmith JI, Slinker JD, Rohl R, Pascal RA, Malliaras GG, Bernhard S (2005) Chem Mater 17:5712
112. VanSlyke SA, Tang CW (1987) Appl Phys Lett 51:913
113. Kim JS, Ho PKH, Greenham NC, Friend RH (2000) J Appl Phys 88:1073
114. Baldo MA, Adachi C, Forrest SR (2000) Phys Rev B 62:10967
115. Hoshino S, Suzuki H (1996) Appl Phys Lett 69:224
116. Mattoussi H, Murata H, Merritt CD, Kafafi ZH (1998) SPIE Proc 3476:49
117. Murata H, Merritt CD, Mattoussi H, Kafafi ZH (1998) SPIE Proc 3476:88
118. Bulovi V, Shoustikov A, Baldo MA, Bose E, Kozlov VG, Thompson ME, Forrest SR (1998) Chem Phys Lett 287:455
119. Lamansky S, Thompson ME, Adamovich V, Djurovich PI, Adachi C, Baldo MA, Forrest SR, Kwong R (2005) Organometallic compounds and emission-shifting organic electrophosphorescence. US Patent 6 939 624

120. Kalinowski J, Stampor W, Cocchi M, Virgili D, Fattori V, Marco P (2004) ChemPhys 39:297
121. Cleave V, Yahioglu G, Le Barny P, Friend R, Tessler N (1999) Adv Mater 11:285
122. Ren X, Li J, Holmes RJ, Djurovich PI, Forrest SR, Thompson ME (2004) Chem Mater 16:4743
123. Pai DM, Yanus JF, Stolka M (1984) J Phys Chem 88:4714
124. Riess W, Beierlein TS, Riel H (2005) In: Brütting W (ed) Physics of organic semiconductors. Wiley, Weinheim (pp 511–527, ISBN 3-527-40550-X)
125. Yersin H (2004) Top Curr Chem 1:241
126. Adachi C, Baldo MA, Forrest SR, Thompson ME (2000) Appl Phys Lett 77:904
127. Berner D, Houili H, Leo W, Zuppiroli L (2005) Phys Stat Sol 9:202
128. Masenelli B, Berner D, Bussac MN, Zuppiroli L (2001) Appl Phys Lett 79:4438
129. Tutis E, Bussac MN, Masenelli B, Carrard M, Zuppiroli L (2001) J Appl Phys 89:430
130. Masenelli JB, Tutis E, Bussac MN, Zuppiroli L (2001) Synth Met 122:141
131. Masenelli JB, Tutis E, Bussac MN, Zuppiroli L (2000) Synth Met 121:1513
132. Pei Q, Yu G, Zhang C, Yang Y, Heeger AJ (1995) Science 269:1086
133. Holder E, Langeveld BMW, Schubert US (2005) Adv Mater 17:1109
134. Pei Q, Yu G, Zhang YC, Yang Y, Heeger AJ (1995) Science 269:1086
135. Chuah BS, Hwang DH, Chang SM, Davies JE, Moratti SC, Li XC, Holmes AB, De Mello JC, Tessler N, Friend RH (1997) SPIE Proc 132:3148
136. Slinker JD, Koh CY, Malliaras GG, Lowry MS, Bernhard S (2005) Appl Phys Lett 86:173506